



The Clumpy Structure of Five Star-bursting Dwarf Galaxies in the MaNGA Survey

Mengting Ju^{1,2} , Jun Yin^{1,3} , Lei Hao¹ , Chenxu Liu⁴ , Chao-Wei Tsai^{5,6,2} , Junfeng Wang⁷ , Zhengyi Shao^{1,3} ,
Shuai Feng^{8,9} , and Yu Rong¹⁰

¹ Key Laboratory for Research in Galaxies and Cosmology, Shanghai Astronomical Observatory, Chinese Academy of Sciences, Shanghai 200030, China
mtju@shao.ac.cn, yyin@shao.ac.cn, haol@shao.ac.cn

² University of Chinese Academy of Sciences, Beijing 100049, China

³ Key Lab for Astrophysics, Shanghai 200034, China

⁴ South-Western Institute for Astronomy Research, Yunnan University, Kunming 650500, China

⁵ National Astronomical Observatories, Chinese Academy of Sciences, Beijing 100101, China

⁶ Institute for Frontiers in Astronomy and Astrophysics, Beijing Normal University, Beijing 102206, China

⁷ Department of Astronomy, Physics Building, Xiamen University, Xiamen, Fujian 361005, China

⁸ College of Physics, Hebei Normal University, Shijiazhuang 050024, China

⁹ Hebei Key Laboratory of Photophysics Research and Application, Shijiazhuang 050024, China

¹⁰ Department of Astronomy, University of Science and Technology of China, Hefei 230026, China

Received 2023 September 27; revised 2023 November 16; accepted 2023 November 27; published 2024 January 31

Abstract

The star-forming clumps in star-bursting dwarf galaxies provide valuable insights into understanding the evolution of dwarf galaxies. In this paper, we focus on five star-bursting dwarf galaxies featuring off-centered clumps in the Mapping Nearby Galaxies at Apache Point Observatory survey. Using the stellar population synthesis software Fitting Analysis using Differential evolution Optimization, we obtain the spatially resolved distribution of the star formation history, which allows us to construct the *g*-band images of the five galaxies at different ages. These images can help us to probe the evolution of the morphological structures of these galaxies. While images of a stellar population older than 1 Gyr are typically smooth, images of a stellar population younger than 1 Gyr reveal significant clumps, including multiple clumps which appear at different locations and even different ages. To study the evolutionary connections of these five galaxies to other dwarf galaxies before their star-forming clumps appear, we construct the images of the stellar populations older than three age nodes, and define them to be the images of the “host” galaxies. We find that the properties such as the central surface brightness and the effective radii of the hosts of the five galaxies are in between those of dwarf ellipticals (dEs) and dwarf irregulars (dIrrs), with two clearly more similar to dEs and one more similar to dIrrs. Among the five galaxies, 8257-3704 is particularly interesting, as it shows a previous starburst event that is not quite visible from its *gri* image, but only visible from images of the stellar population at a few hundred million years. The star-forming clump associated with this event may have appeared at around 600 Myr ago and disappeared at around 40 Myr ago.

Key words: galaxies: dwarf – galaxies: evolution – galaxies: formation – Galaxy: structure

1. Introduction

Dwarf galaxies are the most abundant structures in the universe, and their unique properties offer crucial insights into fundamental astrophysical processes and a broader understanding of galaxy formation and evolution. Star-bursting dwarf galaxies, such as a Blue Compact Dwarf (BCD), are a type of dwarf galaxy with high star formation rates (SFRs). Some star-bursting dwarf galaxies have giant star formation clumps (Elmegreen et al. 2012; Verbeke et al. 2014; Zhang et al. 2020). These galaxies are usually gas-rich and tend to have low metallicities (Hunter & Hoffman 1999; Zhang et al. 2012). Some of them have extremely low metallicities, similar to Population I systems. It is proposed that they are very young with the first generation of star formation or the star formation

in these galaxies occurring in intense bursts separated by extended quiescent periods (Searle & Sargent 1972). Several works confirmed that there are old stellar populations in star-bursting dwarf galaxies (Cairós et al. 2001, 2003; Annibali et al. 2013). This leads us to speculate whether these star-bursting dwarf galaxies, when in the quiescent stage, are connected to other types of dwarf galaxies. Some people have attempted to use galaxy images to investigate these connections (e.g., Papaderos et al. 1996, 2008; Amorín et al. 2009; Meyer et al. 2014; Lian et al. 2015; Rey et al. 2023), by comparing the properties of the underlying old-stellar-population hosts with other dwarf galaxies. For example, some studies (e.g., Amorín et al. 2009; Lian et al. 2015) have reported that the effective radii of the hosts of the starbursting dwarfs are smaller than

those of dwarf irregular galaxies (dIrrs), although such results have not been consistently confirmed by studies using near-infrared images. These studies suffer a substantial challenge in separating the active star formation clumps from the hosts. If the analysis is done on the optical images where the star-forming clumps can be significantly visible, only the regions where the contributions from the star-bursting regions are minimal can be used. This puts a strong limitation on this area of study.

The star formation clumps found in local star-bursting dwarf galaxies, even though there can be contaminants in studies of the hosts, are by themselves valuable in understanding the evolution of these galaxies due to their resemblance to the clumpy structures observed in high-redshift galaxies. High-redshift galaxies are known to be clumpy (Elmegreen et al. 2004; Conselice et al. 2005). The clumps in high-redshift and local galaxies show great similarities, both exhibiting high SFR and low gas-phase metallicity (Erb et al. 2006; Sánchez Almeida et al. 2014, 2018; Lagos et al. 2018), except that clumps in high-redshift galaxies tend to be larger in size compared to those in local galaxies (Genzel et al. 2006; Elmegreen et al. 2013). In Ju et al. (2022, hereafter Ju22), we reported a distinct off-centered clump in the star-bursting dwarf galaxy (8313-1901) in the Mapping Nearby Galaxies at Apache Point Observatory survey (MaNGA; Bundy et al. 2015). The clump has a size comparable to the clumps at high redshifts. By analyzing the SFR, metallicity, kinematics and particularly the stellar populations of the clump, as well as those of the host, we concluded that this clump likely originated from a gas accretion event.

The primary analysis of the clump in 8313-1901 by Ju22 was done on the Integral Field Spectroscopy (IFS) data. Unlike traditional aperture or long slit spectrographs, which provide light within a small region of galaxies, IFS allows simultaneous spectroscopic observations of multiple regions across the field of view (FoV). The spatially resolved spectra can be used to separate the physical properties, such as gas-phase metallicity, stellar populations and star formation history (SFH), in the clump regions and other locations.

Inspired by the analysis of the clump in MaNGA 8313-1901, in this paper, we investigate five MaNGA galaxies, including 8313-1901, selected by their dynamically incoherent star formation clumps with respect to the host galaxies. We study both their hosts and the clumps using a dedicated spectral analysis tool: the Fitting Analysis using Differential evolution Optimization (FADO; Gomes & Papaderos 2017). The paper is structured as follows: In Section 2, we introduce the MaNGA survey data of the five galaxies. In Section 3, we analyze the physical properties of these five dwarfs and their stellar populations. In Section 4, we discuss the structural changes. A summary is presented in Section 5. Throughout this paper, we adopt cosmological parameters of $H_0 = 70 \text{ km s}^{-1} \text{ Mpc}^{-1}$, $\Omega_M = 0.3$ and $\Omega_\Lambda = 0.7$.

2. Data

The MaNGA survey observed approximately 10,000 nearby galaxies ($\langle z \rangle \sim 0.03$). Among them, there were nearly 1500 dwarf galaxies with stellar masses less than $10^9 M_\odot$. We tentatively compile a sample of BCD candidates from the MaNGA survey using the BCD criteria outlined in Gil de Paz et al. (2003) and Sánchez Almeida et al. (2008). The criteria are set to be that these galaxies are blue ($\langle \mu_B \rangle - \langle \mu_R \rangle \leq 1 \text{ mag arcsec}^{-2}$), compact ($\langle \mu_B \rangle < 22 \text{ mag arcsec}^{-2}$) and dwarfy ($M_* < 10^9 M_\odot$). Based on the measurements in the NASA-Sloan Atlas catalog, we identify 53 galaxies that meet these criteria. Approximately half of them exhibit off-center clumps, and among them we select five representative star-bursting dwarf galaxies. Their *gri* composite images from Sloan Digital Sky Survey (SDSS) are shown in the first column of Figure 1.

MaNGA galaxy 8257-3704 is characterized by a distinct clump to the northwest. 8313-1901 features a significant clump to the northeast, which we investigated in detail in Ju22. 8563-3704 has two blue clumps: one to the north and the other to the south. 8615-1901 has a blue clump covering the entire galaxy. 9894-9102 has a sequence of multiple clumps that are close to each other.

Table 1 presents the coordinates, redshifts, $NUV - r$ colors, *g*-band absolute magnitudes, stellar masses, H I gas masses and environmental information of these galaxies. The coordinates, redshifts, $NUV - r$ colors, *g*-band absolute magnitudes and stellar mass are obtained from the NASA-Sloan Atlas catalog. The magnitudes, including *NUV*, *g* and *r*-bands, and the stellar masses are the elliptical Petrosian parameters in the NASA-Sloan Atlas catalog. The H I gas masses in Table 1 are obtained from the HI-MaNGA follow-up survey, which includes information from Green Bank Telescope observations and from the Arecibo Legacy Fast ALFA project (Masters et al. 2019; Stark et al. 2021).

The MaNGA survey is an IFS survey and is a part of the fourth generation of the SDSS (SDSS-IV; Blanton et al. 2017). It employs 17 science Integral Field Units (IFUs) ranging in size from 19 fibers to 127 fibers ($12''$ – $32''$ diameter). The selected IFUs are required to cover the galaxies up to 1.5 and 2.5 effective radii (R_e) (Yan et al. 2016a). The spectra are obtained with the Baryon Oscillation Spectroscopic Survey spectrographs (Smee et al. 2013) on the 2.5 m Sloan Telescope at Apache Point Observatory (Gunn et al. 2006). The typical MaNGA reduced data cubes have a spaxel size of $0''.5$ and a point-spread function (PSF) with a full width at half-maximum (FWHM) of $2''.5$ (Law et al. 2015; Yan et al. 2016a). The MaNGA survey provides data covering a wavelength range from 3600 to 10300 Å with a resolution of $R \sim 2000$ (Law et al. 2016, 2021; Yan et al. 2016b). In this work, we mainly use the data product from the MaNGA Data Reduction Pipeline (DRP) MPL-11 version (Law et al. 2016). The maps of the median signal-to-noise ratio (S/N) of the continuum averaged over the

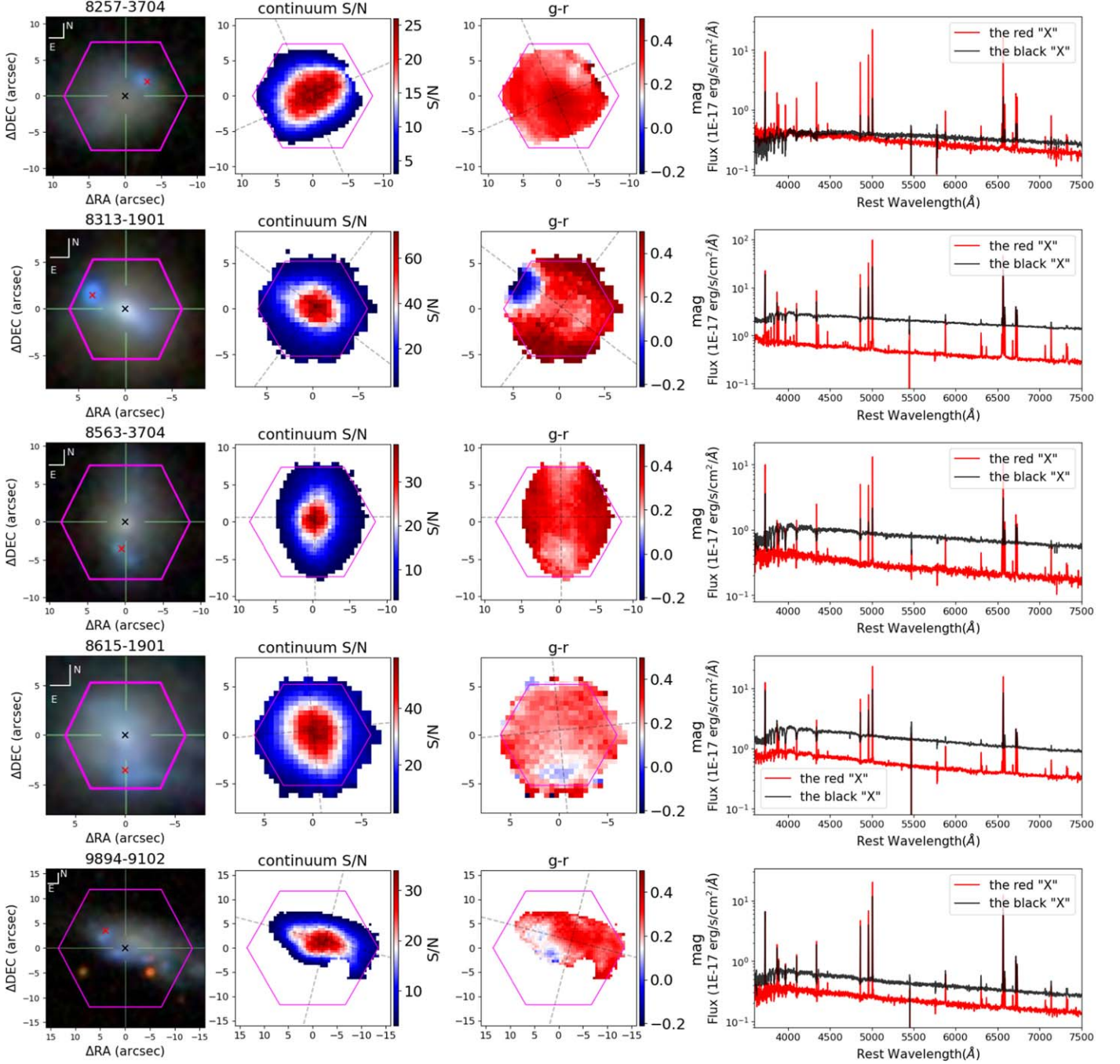


Figure 1. MaNGA plate IFU ID from top to bottom: 8257-3704, 8313-1901, 8563-3704, 8615-1901 and 9894-9102. From left to right: SDSS *gri* composite images, the mean S/N of the continuum between 3600 and 7500 Å, $g-r$ color and two spaxel spectra that are located at the red and black crosses marked in the *gri* composite images. The magenta hexagons in the first three columns display the coverage of the MaNGA bundle. We only show the spaxels with S/N greater than 3. The gray dashed lines in the second and third columns indicate the major and minor axes of each galaxy, which are determined by fitting the two-dimensional surface brightness profiles of the host galaxies, as described in Section 4.1. In the other two-dimensional images presented in this paper, unless otherwise specified, the gray dashed lines represent the major and minor axes of the galaxies. The black curves in the fourth column represent the spectra from the center of the MaNGA FoV, and the red curves show the spectra in the clumps.

wavelength range of $3600 \text{ Å} < \lambda < 7500 \text{ Å}$ are displayed in the second column of Figure 1. In the five galaxies, there are 3839 spaxels with a continuum S/N greater than 3, covering a significant fraction of the observed field (82%). The spectra in

the central regions have S/N of several tens. In this paper, we use only the 3839 spaxels for further analysis.

These spectra suffer a certain amount of extinction by the interstellar medium (ISM) in our Milky Way. Thus, we correct

Table 1
Parameters of the Five Star-bursting Dwarf Galaxies

SDSS	Plateifu	R.A. (J2000) ($^{\circ}$)	Decl. (J2000) ($^{\circ}$)	Redshift ^a	$NUV - r^a$ (mag)	M_g^a (mag)	$\log(M_*)^a$ (M_{\odot})	$\log(M_{H1})^b$ (M_{\odot})
J110212.87+451813.7	8257-3704	165.5536	45.3039	0.0202	2.76	-17.54	8.69	9.36
J160108.90+415250.7	8313-1901	240.2871	41.8807	0.0243	1.40	-18.64	8.88	9.37
J160820.11+494802.4	8563-3704	242.0838	49.8007	0.0192	1.70	-17.57	8.63	...
J212417.32+010142.1	8615-1901	321.0722	1.0284	0.0197	1.30	-18.59	8.77	9.64
J164625.11+194611.5	9894-9102	251.6052	19.7696	0.0232	1.99	-18.59	8.79	9.76

Notes.

^a The NASA-Sloan Atlas catalog: <http://www.nsatlas.org>.

^b Masters et al. (2019), Stark et al. (2021).

all these observed spectra for the Milky Way foreground extinction law of Fitzpatrick (1999) with the Galactic reddening $E(B - V)$ provided by the MaNGA database. We then de-redshift the spectra using the redshift values of the five galaxies provided by the NASA-Sloan Atlas catalog. We refer to these corrected spectra as the corrected-observed (Cobs) spectra. The third column of Figure 1 shows the two-dimensional distribution map of the $g - r$ color synthesized from the Cobs spectra. The magnitudes in g - and r -band are calculated by convolving the Cobs spectra with the filter response curves. It can be seen that the clump regions are generally bluer than the other regions in galaxies which is consistent with the gri composite images. In the fourth column, we present the Cobs spectra of two spaxels in each galaxy marked by the red cross and the black cross in the gri composite images, respectively. The red cross marks a representative position in the clump, while the black cross represents the center of the MaNGA FoV.

3. Results

3.1. The Spectral Fitting Analyses

The MaNGA spectra of the five star-bursting galaxies are analyzed with FADO (Gomes & Papaderos 2017). FADO is a spectral stellar population synthesis tool. Unlike most currently available stellar population synthesis codes, the fitting of the stellar continuum in FADO does not mask nebular emission lines. Instead, it incorporates self-consistent observed nebular emission (both nebular continuum and emission lines) that is based on the SFH and chemical enrichment history inferred from the best stellar models. The nebula continuum is formed when the Lyman continuum photons ($\lambda < 911.76 \text{ \AA}$) emitted by the stars are absorbed by the H II region gas and re-emitted at longer wavelengths. In FADO, the spectrum of the nebular continuum is included in the fitting, assuming case B recombination under typical physical conditions of the H II region, i.e., an electron density of $n_e = 100 \text{ cm}^{-3}$ and temperature of $T_e = 10^4 \text{ K}$. Nebular emission can significantly contaminate the host continuum photometry in the star-forming

galaxies, and further affect spectral energy distribution (SED) studies (Salzer et al. 1989; Jaskot & Oey 2013). It is crucial to remove the contribution of nebular emission from the stellar continuum SED of star-forming regions; otherwise old stellar populations might be overestimated (Izotov et al. 2011). Pappalardo et al. (2021) compared the results of FADO with two other spectral stellar population synthesis models, on a set of simulated galaxy spectra which were constructed as having both stellar and nebular emissions. For the two models that do not include the nebular emissions in the fitting, the mass-weighted mean age obtained is overestimated by ~ 2 dex at a young stellar age, if the contributions of nebular emissions are not considered in the spectra.

We use FADO (v. 1B) to fit the 3839 Cobs spectra, covering the wavelength range from 3600 to 7500 \AA and estimating the host galaxy extinction using the extinction law of Calzetti (2001). We choose single stellar populations (SSPs) from Bruzual & Charlot (2003, hereafter BC03) which were built on the Padova1994 stellar evolution tracks (Fagotto et al. 1994a, 1994b) and the Salpeter initial mass function (IMF). A combination of 90 SSPs with 18 ages (age = 1.00 Myr, 1.58 Myr, 2.51 Myr, 3.98 Myr, 6.31 Myr, 10.00 Myr, 15.85 Myr, 25.12 Myr, 40.00 Myr, 64.05 Myr, 101.52 Myr, 160.90 Myr, 255.00 Myr, 404.15 Myr, 640.54 Myr, 1.02 Gyr, 3.75 Gyr and 15.00 Gyr, ranging from 1 Myr to 15 Gyr) and five metallicities ($Z = 0.0004, 0.004, 0.008, 0.02, \text{ and } 0.05$) is used.

Figure 2 presents the FADO fitting results for the five galaxies. From top to bottom, we show the best-fit spectrum in a representative spaxel in the clump region of 8257-3704, 8313-1901, 8563-3704, 8615-1901 and 9894-9102, respectively. The orange curve represents the Cobs spectrum. The best-fit continuum is displayed in blue. The continuum consists of the stellar continuum (black) and the nebular continuum (purple). The right panels of Figure 2 show the fraction of stellar mass of each SSP that constitutes the best-fitting populations in the age-metallicity maps (the top panels) and in the SFH (the bottom panels). The stellar continua can be reconstructed with the SFH and the 90 SSPs.

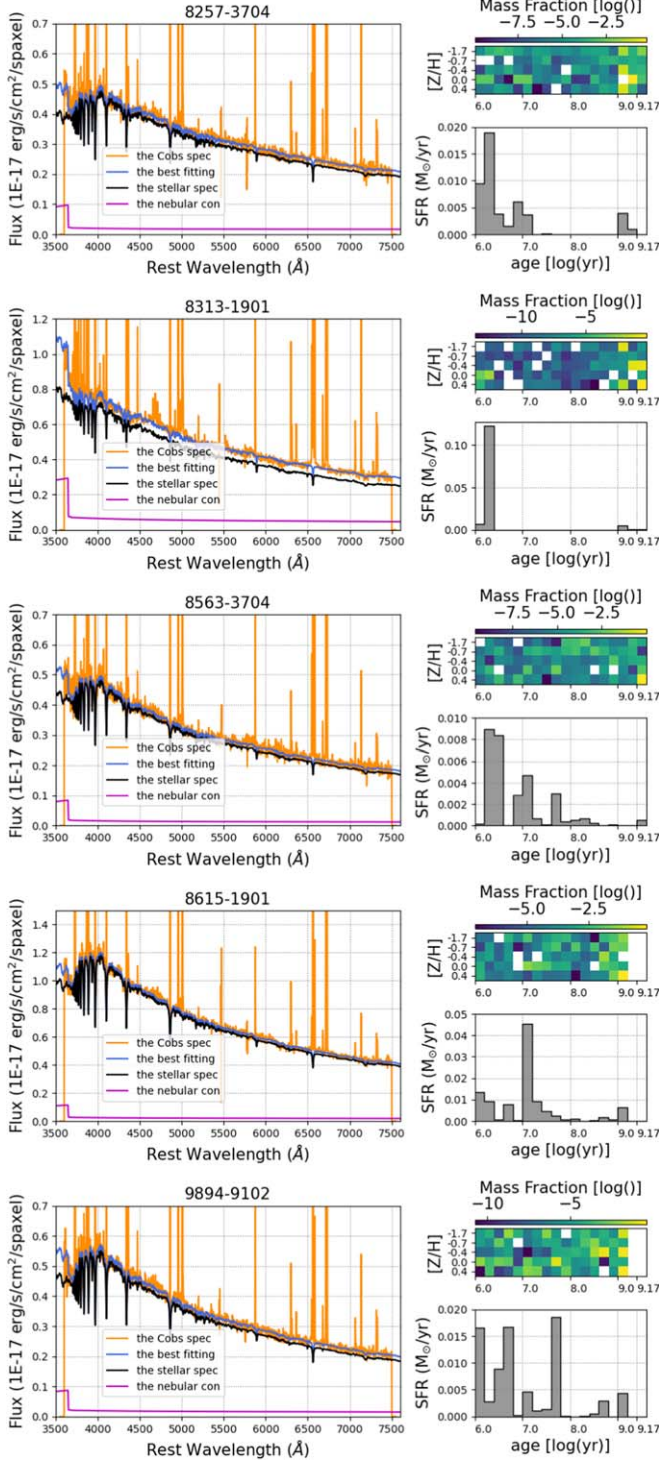


Figure 2. Examples of the FADO fitting results for the five galaxies. The orange lines in the left panels show the Cobs spectra in clump regions. The blue lines are the best-fit continuum. The black lines are the stellar continuum. The purple lines are the nebular continuum. The right panels display the contributions of SSPs that form the best-fit populations in the age–metallicity maps (top) and the evolution of SFR (bottom), normalized by stellar mass.

In Figure 2, we find that the nebular continuum in the best-fit result does have a non-zero contribution. In Figure 3, we investigate the nebular emission in detail, calculating the nebular contributions of each galaxy. In the top row of Figure 3, we show the g -band images of the nebular continua and the unit is nanomaggies. The middle row features the ratio of the nebular continua to the overall continua in g -band flux. The nebular continua contributions are nearly 5% in the clump regions in most of the five galaxies. 8313-1901, which exhibits the highest SFR in the five star-bursting galaxies, has a higher nebular contribution ($\sim 10\%$) compared to the other four galaxies. The bottom row in Figure 3 displays the ratio of the g -band flux from the nebular emissions, including the nebular continuum and emission lines to the g -band flux from the Cobs spectra. The nebular emission contributions are significant, from 30% to 60%, to the optical flux in the clump regions. This is consistent with the findings of other studies (e.g., Krueger et al. 1995).

We check FADO results with our previous findings in Ju22. In Ju22, we constructed the clump spectrum in 8313-1901. The clump spectrum is obtained by subtracting the observed spectrum from the host contribution. It matches very well with the young model spectrum (≤ 7 Myr), which has stellar mass of $\log(M/M_\odot) = 6.26$. We use FADO and 90 SSP models to fit the clump spectrum. The FADO results, including the stellar populations and stellar mass, are consistent with the results of Ju22. The stellar population is very young (~ 4 Myr) and the stellar mass is about $\log(M/M_\odot) = 6.12$.

3.2. SFR, Gas-phase Metallicity and Kinematics

With the emission-line flux, we estimate the SFR and gas-phase metallicity of the five star-bursting galaxies. We select the spaxels whose S/N of the $H\alpha$ emission line are higher than 15, and we find nearly all of these spaxels fall into the star-forming region in the Baldwin–Phillips–Terlevich diagram ($[N\text{ II}]/H\alpha$ versus $[O\text{ III}]/H\beta$; Baldwin et al. 1981; Kewley et al. 2001; Kauffmann et al. 2003). SFR is calculated with the $H\alpha$ luminosity following (Hao et al. 2011; Kennicutt & Evans 2012)

$$\log\left(\frac{\text{SFR}}{M_\odot \text{ yr}^{-1}}\right) = \log\left(\frac{L_{H\alpha}}{\text{erg s}^{-1}}\right) - 41.27. \quad (1)$$

The SFR maps are depicted in the first column of Figure 4. There are clumps with high star formation in all five galaxies. Some have multiple off-centered clumps. Based on the peak positions of the clumps identified in the SFR maps, we label them with black, orange and red circles. These circles are centered at the locations with the highest SFR within each clump, and their diameters are $2''.5$. For the galaxies with multiple clumps, the central SFR decreases from black circles to orange circles to red circles.

There are a lot of methods to calculate the oxygen abundance (Pagel et al. 1979; Storch-Bergmann et al. 1994; Denicolò

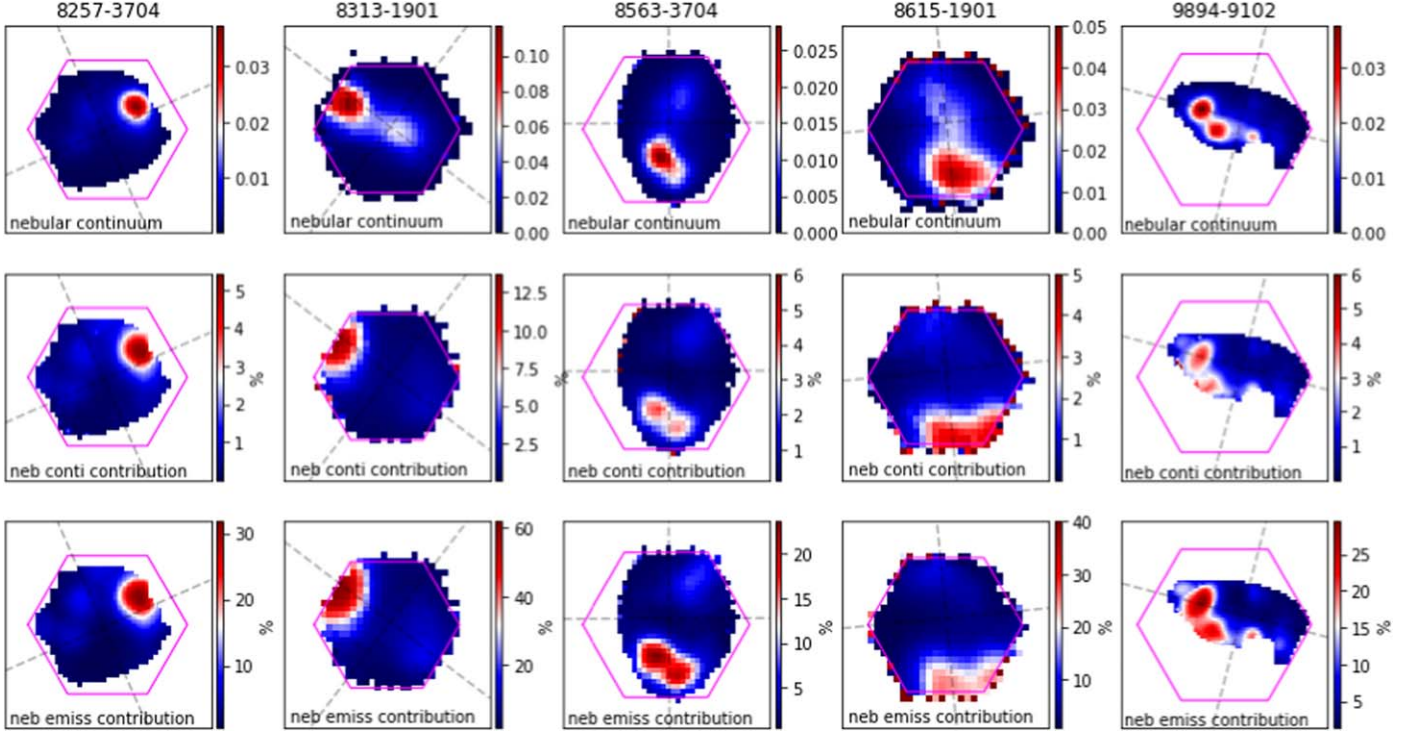


Figure 3. Top row: the g -band flux of nebular continua. Middle row: the percentage of the flux of the nebular continua in the overall continua. Bottom row: the percentage of the flux of the nebular emission contributing to the Cobs spectra.

et al. 2002; Pettini & Pagel 2004; Tremonti et al. 2004; Henry et al. 2013; Marino et al. 2013). In this work, we estimate the metallicity of the spaxels using the calibration obtained for the O3N2 indicator by Marino et al. (2013) (Equation (2)). The O3N2 indicator depends on two strong emission line ratios (Alloin et al. 1979) (Equation (3))

$$12 + \log(\text{O}/\text{H}) = 8.533[\pm 0.012] - 0.214[\pm 0.012] \times \text{O3N2}, \quad (2)$$

where

$$\text{O3N2} = \log \frac{[\text{O III}] \lambda 5007 / \text{H}\beta}{[\text{N II}] \lambda 6584 / \text{H}\alpha}. \quad (3)$$

The second column of Figure 4 displays the metallicity maps. In general, the clumps show poor metallicities, which are lower by about 0.1 dex than those of the host galaxies. In galaxies with multiple clumps, there is an inverse relationship between SFR and metallicity, where higher SFR corresponds to lower metallicity. There are some exceptions; for example, 8615-1901 has two low-metallicity regions, with one of them not exhibiting strong SFR.

The gas velocity maps can help us determine if there is any disturbance in the clump regions compared to the gas in the host galaxy. We obtain the observed $\text{H}\alpha$ velocity maps from the Data Analysis Pipeline (Belfiore et al. 2019; Westfall et al. 2019), and plot them in the third column of Figure 4. We find

that generally these galaxies have rotation-dominated velocity fields. 8313-1901, 8563-3704 and 8615-1901 have clear disturbances in the position of the clumps, indicating that the clumps in them might have external origins.

3.3. g -band Images in Different Age Intervals

The FADO fitting analysis of the IFS data provides spatially resolved stellar populations. This enables us, in principle, to reconstruct the distribution of stellar fluxes (i.e., the images) at different ages, allowing us to probe how the morphologies of the galaxies can change as a function of evolutionary time (Peterken et al. 2019). We attempt to conduct this investigation in this subsection.

Based on the spatially resolved SFH and $E(B - V)$ values obtained by FADO, we use 90 SSPs to model the attenuated stellar continua for four age intervals at each spaxel: 0–10 Myr (young), 10–100 Myr (intermediate young), 100 Myr–1 Gyr (intermediate old) and ≥ 1 Gyr (old). After convolving the g -band filter with the Python code SEDPY (Johnson 2019) in unit of nanomaggies,¹¹ we get the g -band images of five galaxies in four age intervals, as shown in Figure 5. All g -band seeing-limited images are smoothed using a Gaussian profile with $\text{FWHM} = 2''.5$ for uniform resolution and the positions of the

¹¹ $\sim 3.631 \mu\text{Jy}$; see <https://www.sdss.org/dr17/algorithms/magnitudes/>.

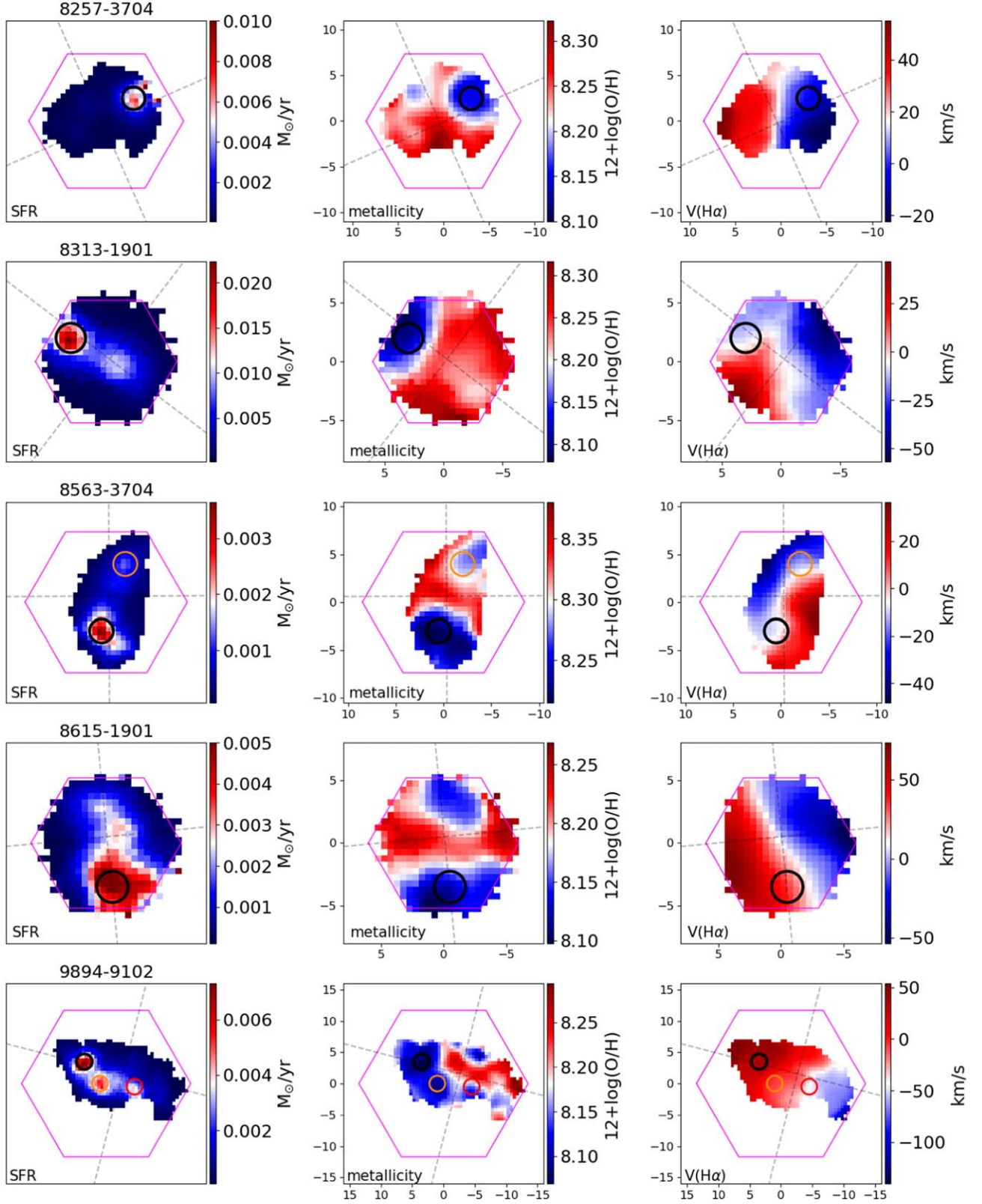


Figure 4. From left to right: the SFR maps, the metallicity maps and the $\text{H}\alpha$ velocity maps. The black circles, orange circles and red circles with diameters of $2''.5$ mark the clumps in the five star-bursting galaxies.

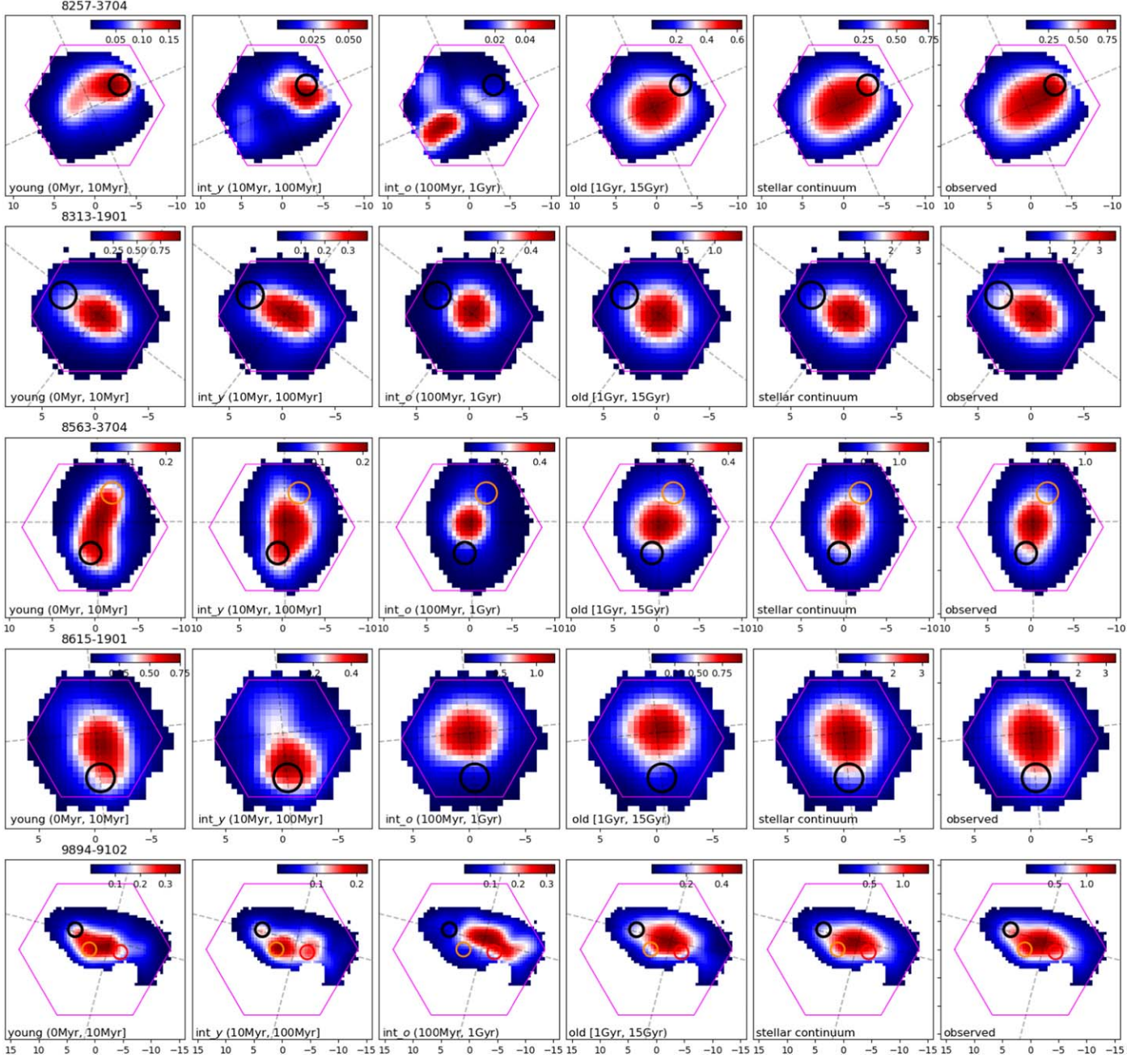


Figure 5. The smoothed g -band images of the five galaxies. The unit is nanomaggies. From left to right are the images of young stellar populations (0–10 Myr), intermediate-young stellar populations (10–100 Myr), intermediate-old stellar populations (100 Myr–1 Gyr) and old stellar populations (≥ 1 Gyr), along with the stellar images and the observed images.

clumps are marked with circles, as in Figure 4. The first to the fourth columns are the reconstructed g -band images of young stellar populations, intermediate-young stellar populations, intermediate-old stellar populations and old stellar populations, respectively. We also calculate the g -band stellar images based on the attenuated stellar continua predicted by FADO and show them in the fifth column of Figure 5. The observed images

derived from the Cobs spectra are displayed in the sixth column for comparison. Like the previous images from the four age intervals, both the stellar images and the observed images are smoothed.

The structures of the g -band images of the five galaxies in different age intervals are clearly different from each other. In particular, the images of young, intermediate-young and

intermediate-old stellar populations are more clumpy and asymmetric compared to the images of old stellar populations. This implies that the clumps in the five star-bursting dwarf galaxies only appeared within the past few hundred million years. This finding is in agreement with previous studies (Tosi 2009; McQuinn et al. 2010). The morphology of the images of old stellar populations is similar to that of the stellar images, primarily because the *g*-band flux of the old stellar populations is generally greater than that of the younger stellar populations in most galaxies. Below, we provide a detailed description of these images for each galaxy.

1. 8257-3704: An off-centered clump with high SFR and low metallicity is shown to the northwest in the *gri* image in the first column of Figure 1. This clump is visible in both the images of young and intermediate-young stellar populations but not in other age intervals. Additionally, we have identified a clump in the southeastern part of the galaxy in the image of intermediate-old stellar populations. The southeastern clump exhibits slightly lower metallicity compared to the host galaxy, although it is not clearly distinguishable in the *gri* composite image and the SFR map. The image of old stellar populations is more circular than the overall stellar image, indicating that the flux contribution of the young populations in this galaxy cannot be ignored. We speculate that this galaxy may have experienced two star formation events within a few hundred million years, with the first one occurring in the southeast and the second one in the northwest.
2. 8313-1901: A distinguishable clump with high SFR and low metallicity is shown in the northeast direction. The morphology of the image of young stellar populations and the observed image is both irregular, while the shape of the galaxy is more symmetric in other age intervals. Our previous analysis indicates that the structural changes of 8313-1901 mainly result from the gas accretion within the recent 7 Myr (Ju et al. 2022).
3. 8563-3704: Two clumps are visible in the north and south directions in the *gri* composite image. They have a high SFR and low metallicities. The gas appears to be kinematically separated from the rotating disk of its host galaxy, as observed in the $H\alpha$ velocity map (the third column of Figure 4). The southern clump is present in both the images of young and intermediate-young stellar populations, while the northern clump is also visible in the image of intermediate-old stellar populations. This suggests that the formation epochs of these two clumps are different, with the northern clump forming first and the southern clump forming subsequently.
4. 8615-1901: In the *gri* composite image, the off-centered clump extends across almost the entire host galaxy. The bluest region in the southern direction of the galaxy exhibits high SFR and low metallicity. The rotation

velocity of the gas is the highest among the five galaxies. The orientation of the clump extension changes across different age intervals. In the image of young stellar populations, the peak is located at the galaxy center and extends toward the south. In the images of intermediate-young stellar populations, the peak is located in the south and extends toward the north. In the image of intermediate-old stellar populations, the peak is at the galaxy center and extends to the east. The morphology of the image of old stellar populations shows symmetry. Both the stellar image and the observed image are asymmetric due to the bluest regions of the galaxy.

5. 9894-9102: In the *gri* composite image, three clumps are observed from east to west. These clumps have high SFR and low metallicities. From east to west, the intensity of star formation in these clumps increases, while the metallicity decreases. Their sequential appearance in the images of intermediate-old, intermediate-young and young stellar populations suggests that these clumps might have formed sequentially from east to west over hundreds of millions of years.

4. Discussion

4.1. The Properties of the Hosts as they Evolve

In Figure 5, we find that there are clear variations in the morphology among images of different stellar populations of the five star-bursting dwarf galaxies. Star-forming clumps only “appear” in younger stellar populations. These hint at us that we may be able to use the images of the different stellar ages to trace how these galaxies evolve. In particular, one of the big interests people have on these dwarf galaxies is to find out whether they could be evolutionarily connected to other types of dwarf galaxies if they had not been star-forming. Previously this could be done on optical images by masking out the star-forming regions and considering what was left as hosts. Now we can look back at the time before the star formation happened, thereby making use of the full image of the galaxy.

In addition, there may be multiple epochs of star formation. The star-forming clumps that appeared earlier may evolve and eventually become a part of the host galaxies. Therefore, we can consider several stages of the “hosts.” We select three age nodes (10 Myr, 100 Myr and 1 Gyr) as the representative formation epochs of star formation, then we can construct the images with stellar populations larger than these three age nodes all as the host galaxies, and name them “old1” (≥ 10 Myr), “old2” (≥ 100 Myr) and “old3” (≥ 1 Gyr) respectively.

The *g*-band images of “old1” (left), “old2” (middle) and “old3” (right), which are smoothed by a Gaussian profile with an FWHM of $2''.5$, are shown in Figure 6. These images are almost all smooth and asymmetric. We use GALFIT to obtain the structure of the images (Peng et al. 2002, 2010). This

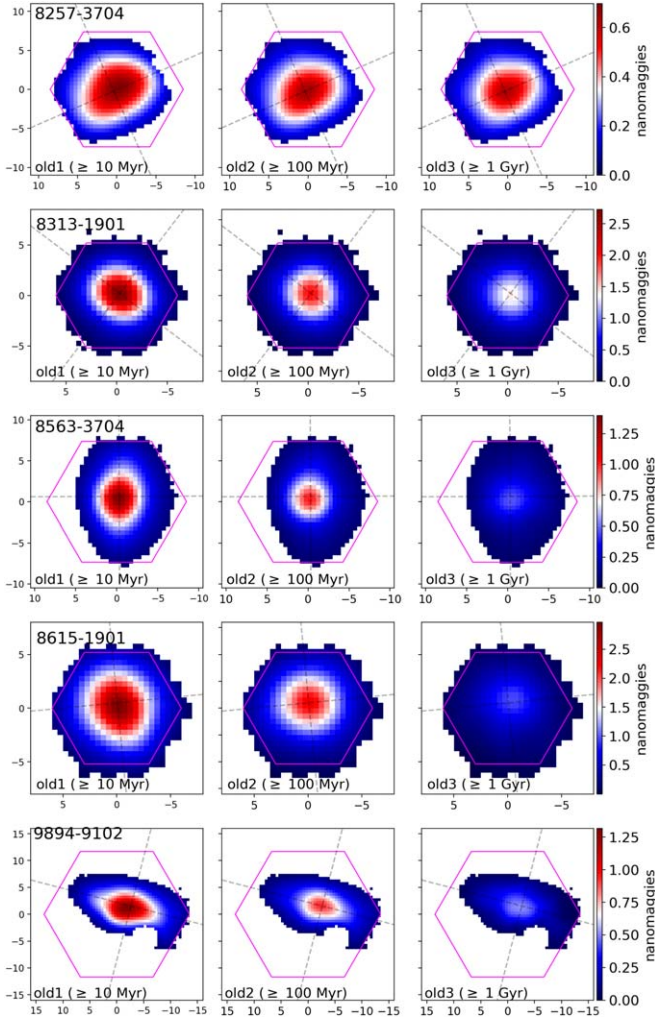


Figure 6. From left to right columns are the old1 images, old2 images and old3 images.

software models the observed light distribution of a galaxy with a best-fit model image convolved with a PSF function. We use a single Sérsic profile to fit the observed images, the stellar images, the old1 images, the old2 images and the old3 images. In Figure 7, we display the fitting results for 8257-3704. The first column comprises the observed image, followed by the stellar image, the old1 image, the old2 image and the old3 image. The second column shows the model images, while the third column displays the residuals. The fitting results for the remaining four galaxies can be found in Appendix. The major and minor axes of the galaxies are depicted as gray dashed lines in the images in this work, which are determined based on the structural parameters derived from the old2 images.

In Figure 8, we show the central surface brightness (μ_0), the effective radius (R_e) and the Sérsic index (n) of the images of the old1, old2 and old3, stellar images and the observed images. Different lines represent different galaxies. The central surface brightnesses of the five star-bursting dwarf galaxies are

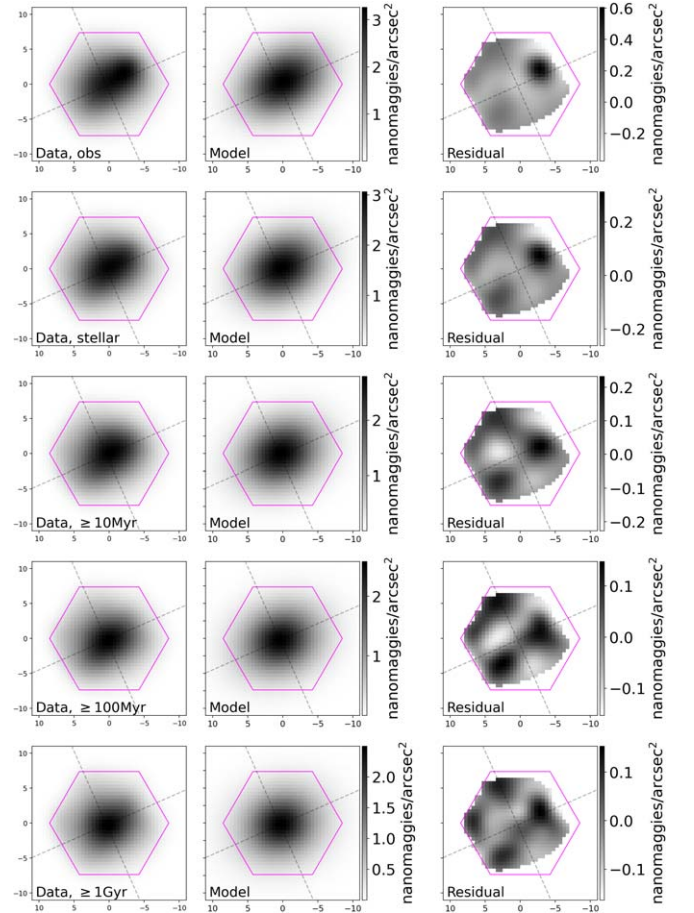


Figure 7. Two-dimensional surface brightness modeling of 8257-3704 with GALFIT. The first column shows the smoothed g -band images from the Cobs spectra and stellar continuum, as well as the old1, old2 and old3 images. The second column displays the best GALFIT fitting model images. The third column depicts the residual images.

generally brighter as they evolve, some can increase over $1 \text{ mag arcsec}^{-2}$. Comparatively, the effective radius and the Sérsic index show no significant changes over time. This is probably not as surprising as it looks. One possible reason that we do not observe a clear growth in the size of the disk for these galaxies is that the images are reconstructed from the MaNGA IFU data and have limited spatial resolution. Another more likely reason is related to the fact that the images we construct for different stellar ages represent how these stellar populations are distributed now, not when they were born. In the early stages of galaxy formation, galaxies tend to exhibit a clumpy morphology due to continuous gas inflow, as studied by Ceverino et al. (2010). This continuous gas supply maintains a system characterized by a clumpy disk and bulge, which stays in a relatively stable state for several billion years. However, due to various stellar kinematic processes, such as disk rotation and stellar migration, the current appearance of

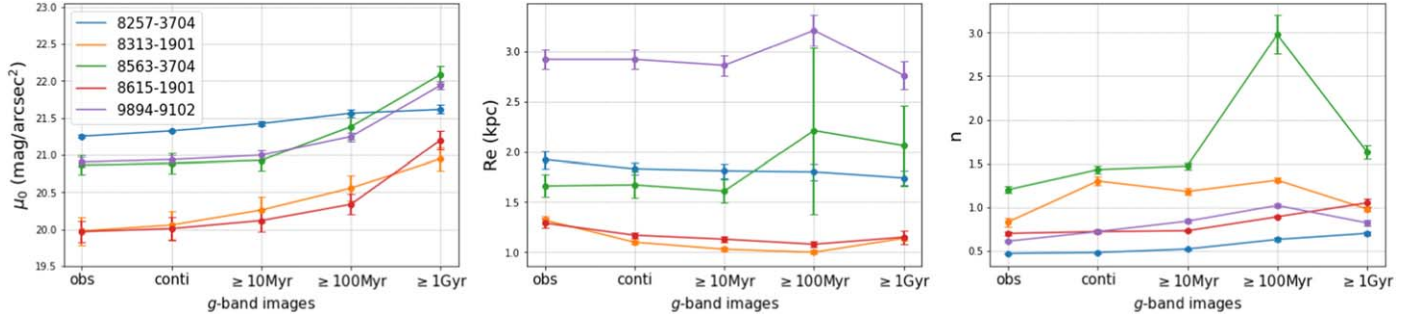


Figure 8. The variation of the structural parameters (central surface brightness μ_0 , left; effective radius R_e , middle; and Sérsic index n , right) in the image sequence of the observed spectra, the stellar continuum, as well as the old1, old2 and old3 images.

galaxies is smoother than their initial state (Mo et al. 2010). As a result, the distribution of stars formed within galaxies may differ from what we observe today. These star-bursting dwarf galaxies might have been more compact than what we currently observe, even for older stellar populations.

On the other hand, the images of different stellar populations of these star-forming dwarf galaxies as they would have evolved until now are perfect to be used to compare with other types of dwarf galaxies to probe possible evolutionary connections among them. Previous studies fitted the surface brightness profile of the host galaxies and then compared the B -band central surface brightness ($\mu_{0,B}$) and the effective radius (R_e) with their absolute B -band magnitudes (e.g., Amorín et al. 2009; Lian et al. 2015). In Figure 9, we construct a similar diagram and compare the structural parameters of these five galaxies with dwarf elliptical galaxies (dEs) and dwarf irregular galaxies (dIrrs) in different absolute magnitude bins in the B -band. We adopt parameters of dEs from Binggeli & Cameron (1993), Graham & Guzmán (2003) (orange crosses) and dwarf dIrrs from van Zee (2000) (black triangles). The central surface brightness and total magnitudes in the r -band for the five star-bursting galaxies are also measured. The magnitudes in r -band are converted into those in B -band following Smith et al. (2002). The five star-bursting galaxies are shown as stars, each in a different color. For a given galaxy, the absolute magnitude values in increasing order are obtained from the observed image, the stellar image, the old1 image, the old2 image and the old3 image. The central brightness ($\mu_{0,B}$, the upper panel) and the effective radius (R_e , the bottom panel) of the old images of the five star-bursting dwarfs fall between those of dEs and dIrrs. 9894-9102 (purple stars) appears to be closer to dIrrs, while 8313-1901 (orange stars) and 8615-1901 (red stars) are more similar to dEs in terms of their central surface brightness and effective radii. In our previous work (Ju22), we proposed that 8313-1901 experienced gas accretion around 7 Myr ago. Combined with the information we obtain here, we speculate that 8313-1901 might have initially been a dwarf elliptical galaxy before the gas accretion event.

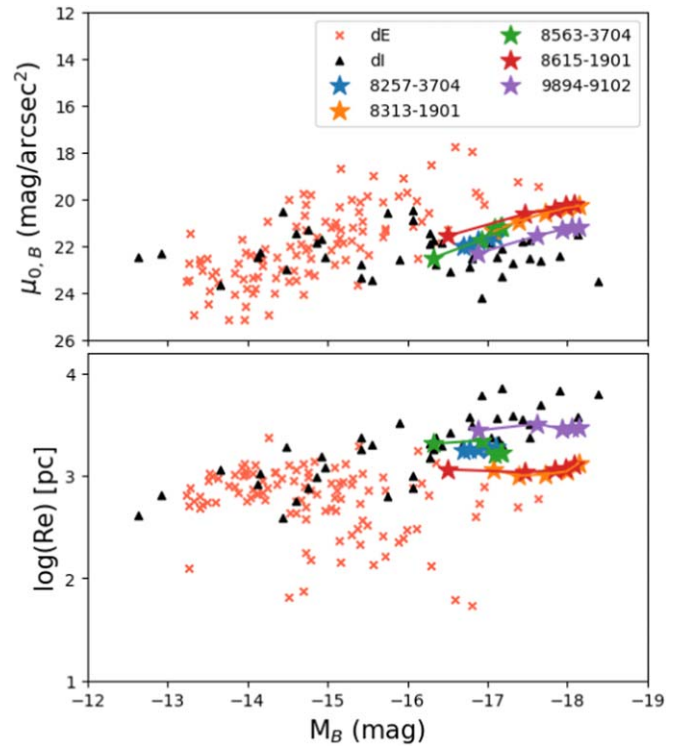


Figure 9. The central surface brightness (μ_0 , the upper panel) and effective radius (R_e , the bottom panel) vs. the B -band absolute magnitudes of galaxies of different types. The orange crosses and black triangles represent the dEs (Binggeli & Cameron 1993; Graham & Guzmán 2003) and dIrrs (van Zee 2000), respectively. The stars in different colors are the five star-bursting galaxies studied in this work. Each galaxy is plotted as five stars that indicate their different B -band absolute magnitudes. The brightest star corresponds to the observed spectra, followed by the stellar continuum, the old1 image, the old2 image and the faintest star represents the old3 image.

4.2. The Clump Evolution in 8257-3704

Figure 5 illustrates that off-centered clumps are generally present in the images of the young, intermediate-young and intermediate-old stellar populations. Considering that these images reflect how the corresponding stellar populations are

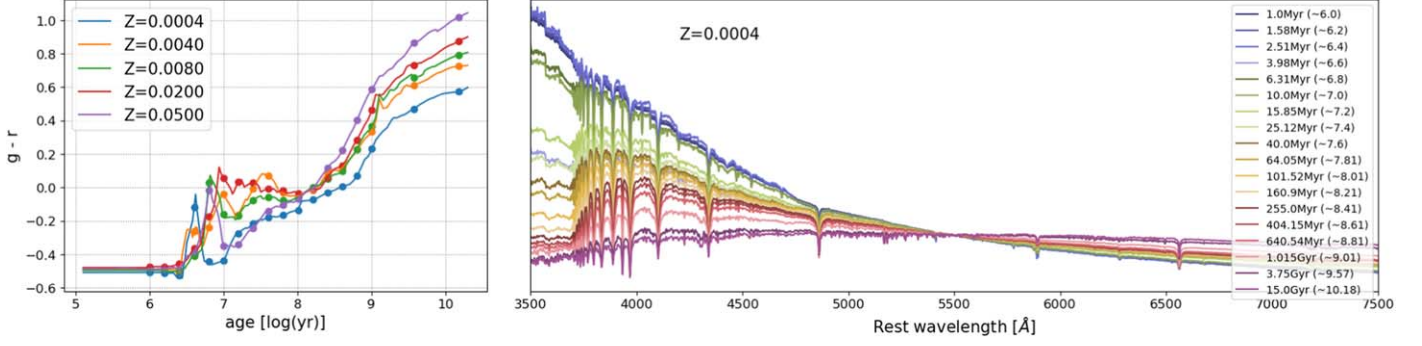


Figure 10. Left: the $g - r$ color of SSPs in the BC03 library. Dots mark the eighteen ages we used in this work. Right: the spectra of the SSPs we used, represented by the stellar metal abundance of 0.0004.

distributed now, not when they were born, the fact that these star-forming clumps remain visible for several hundred million years suggests that the clumps are relatively stable structures and do not easily disintegrate and become part of the disk within a billion years. This suggests that the spatially resolved images of different stellar populations are suitable for studying the properties of the clumps, at least for the last billion years. Among the five galaxies, 8257-3704 stands out as it exhibits two different off-centered clumps in different locations. In the intermediate-old image, the clump is situated in the southeast direction, while in the intermediate-young and young images, it appears in the northwest direction. The southeastern clump is not clear in the gri image. This suggests that 8257-3704 underwent two distinct starburst events: the first one occurred in the southeast direction between 100 Myr and 1 Gyr ago, and it seems to have diminished in the 10–100 Myr. The second starburst took place in the northwest direction and likely occurred within the past 100 Myr. In this subsection, we attempt to check the stellar images of more refined age intervals to further probe when the southeastern clump might have emerged and vanished.

We choose to use the 18 age nodes in the 90 SSPs that we used in this work. To double-check whether this set of age sampling is appropriate, in Figure 10, we plot the $g - r$ colors of the 90 SSPs (left panel) and the spectra of the 18 SSPs with a representative metallicity of $Z = 0.0004$ (right panel). In the left panel, the lines of various colors correspond to different stellar metallicities, while the solid data points signify the 18 ages of the SSPs. In the right panel, the SSPs are normalized to the flux at 5500 Å. We observe that SSPs from 10 Myr to 1 Gyr (including 11 age nodes) can be easily distinguished based on their $g - r$ colors and spectral characteristics. Thus, we will mainly do our investigations on the 11 age nodes.

Given the smaller age intervals, we would also like to check that a reasonable result can be obtained by the FADO fitting of a spectrum of a certain age without confusing two adjacent age nodes. Therefore, we run a simulation test to examine how

Table 2
Checking the Age Robustness Using FADO

Central Age (Myr)	Bin Width (Myr)	FADO Age (Myr)
10.00	8.00–12.00	9.63 ± 0.00
15.85	12.68–19.02	15.29 ± 0.00
25.12	20.09–30.15	25.05 ± 0.00
40.00	32.00–48.00	40.00 ± 0.00
64.05	51.24–76.86	64.03 ± 0.00
101.52	81.21–121.83	118.10 ± 0.01
160.90	128.72–193.08	160.90 ± 0.00
255.00	204.00–306.00	264.40 ± 0.00
404.15	323.32–282.98	404.00 ± 0.00
640.54	512.43–768.65	640.50 ± 0.00
1015.19	812.15–1218.23	1015.00 ± 0.00
20.00	16.00–24.00	20.33 ± 0.00
50.00	40.00–60.00	53.13 ± 0.00
500.00	400.00–600.00	545.10 ± 0.02
10.00	5.00–15.00	10.98 ± 0.00
15.85	7.93–23.77	16.84 ± 0.00
25.12	12.55–37.68	25.07 ± 0.00
40.00	20.00–60.00	39.43 ± 0.00
64.05	32.02–96.07	58.45 ± 0.00
101.52	50.76–152.28	113.60 ± 0.02
160.90	80.45–241.35	165.10 ± 0.00
255.00	127.50–382.50	263.00 ± 0.00
404.15	202.07–606.22	411.00 ± 0.03
640.54	320.27–960.81	659.40 ± 0.06
1015.19	507.59–1522.78	1659.00 ± 1.40
20.00	10.00–30.00	19.90 ± 0.00
50.00	25.00–75.00	59.50 ± 0.00
500.00	250.00–750.00	506.70 ± 0.01

FADO can reproduce the 11 age nodes from 10 Myr to 1 Gyr fed to FADO to fit.

We construct a series of toy-simulated spectra featuring a continuous SFR within specific age intervals. These intervals include the aforementioned 11 age nodes, as well as three ages

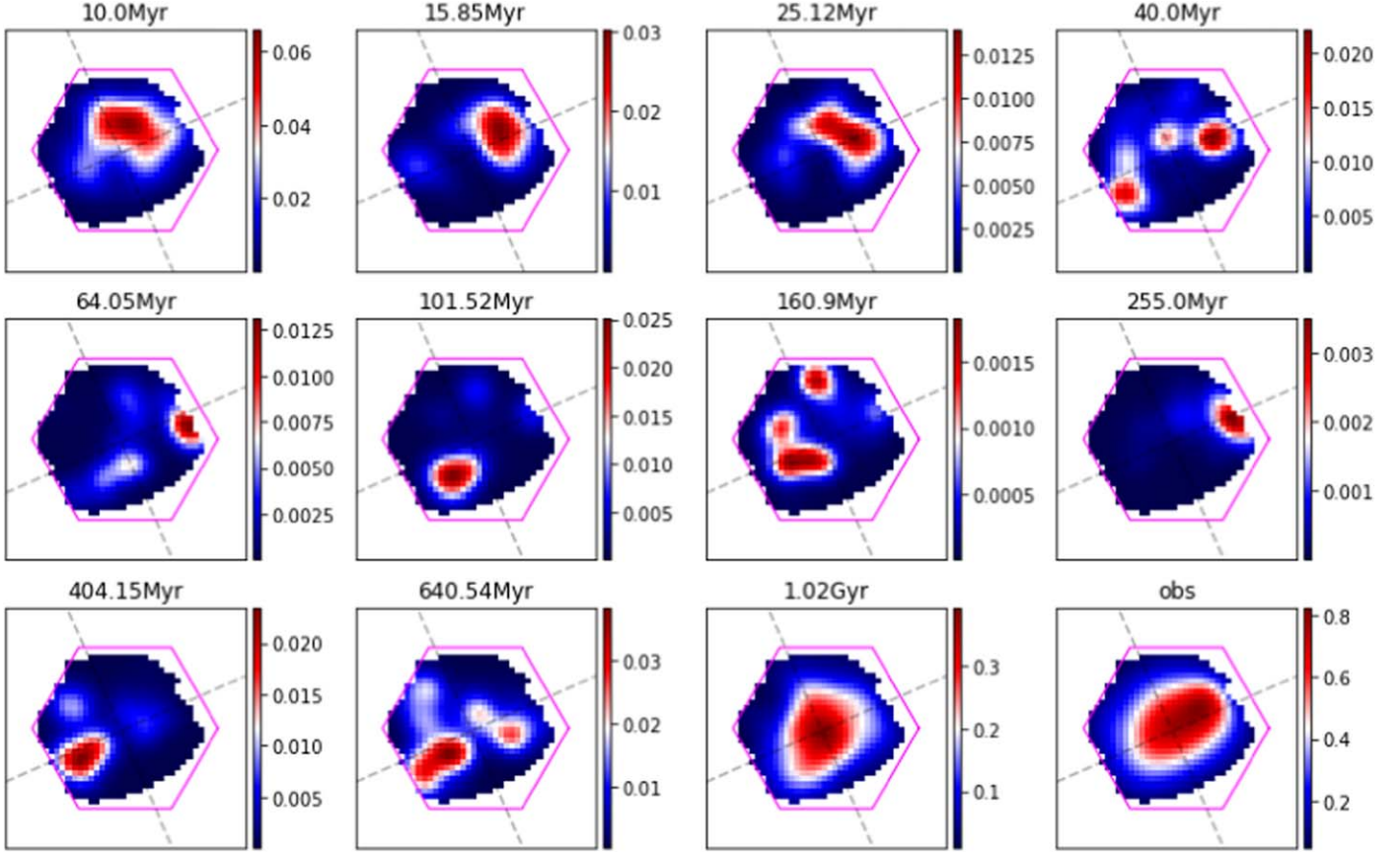


Figure 11. The smoothed g -band images of stellar populations of 8257-3704 at 11 different age intervals, as well as the observed image (bottom-right panel). The units in these images are all nanomaggies.

that were randomly chosen. The simulated spectra are built with 221 SSPs in the BC03 library. These SSPs use the Padova1994 stellar evolution tracks and Chabrier IMF with a metallicity of 0.004. We note that the SSPs used in generating the simulated spectra are different from the ones used in the FADO fitting. In Table 2, we show the central age (C) and bin width (W) in the first column and second column, respectively. Two bin widths regulated by the central age are tested: $W = C \times (1 + 0.2) - C \times (1 - 0.2)$ and $W = C \times (1 + 0.5) - C \times (1 - 0.5)$. The SFR in this age range is $1 M_{\odot} \text{ yr}^{-1}$, and the mass-weighted stellar ages of simulated spectra are the center ages.

We employ FADO and 90 SSPs to fit the simulated spectra. The best-fit mass-weighted mean ages obtained from FADO are presented in the third column of Table 2. Comparing these mass-weighted mean stellar ages with the central ages, we find that the mean ages derived from FADO closely match the central ages, differing by no more than 5% for both bin widths. So, we think the SSPs used in the FADO fitting can distinguish the 11 age nodes we adopt.

We plot the smoothed g -band flux maps of stellar populations across 11 age nodes ($\text{age} = t_n$), ranging from

10 Myr to 1 Gyr in Figure 11. The g -band images from ~ 100 Myr to ~ 640 Myr reveal a distinct clump located in the southeastern region, while the images of the stellar populations younger than 40 Myr clearly present the northwest clump. We also generate a series of g -band images for intervals younger than these age nodes ($\text{age} \leq t_n$). To quantify the clumpy structures observed in these images, we calculate the clumpiness (S) parameter, which is a component of the CAS (Concentration C , Asymmetry A , and Clumpiness S) parameters. The CAS parameters are used for assessing structures and morphology of galaxies (Conselice 2003; Lotz et al. 2004). Clumpiness (also called smoothness) is used to describe the distribution of substructures in galaxy images as defined in Equation (4)

$$S = \frac{\sum_{i,j} |I(i,j) - I_S(i,j)|}{\sum_{i,j} |I(i,j)|}, \quad (4)$$

where $I(i,j)$ is the original image. $I_S(i,j)$ is an image that has been smoothed by convolving the original image with a box of a given width. A smaller S value indicates fewer substructures. We evaluate the formation time of the off-centered clump in

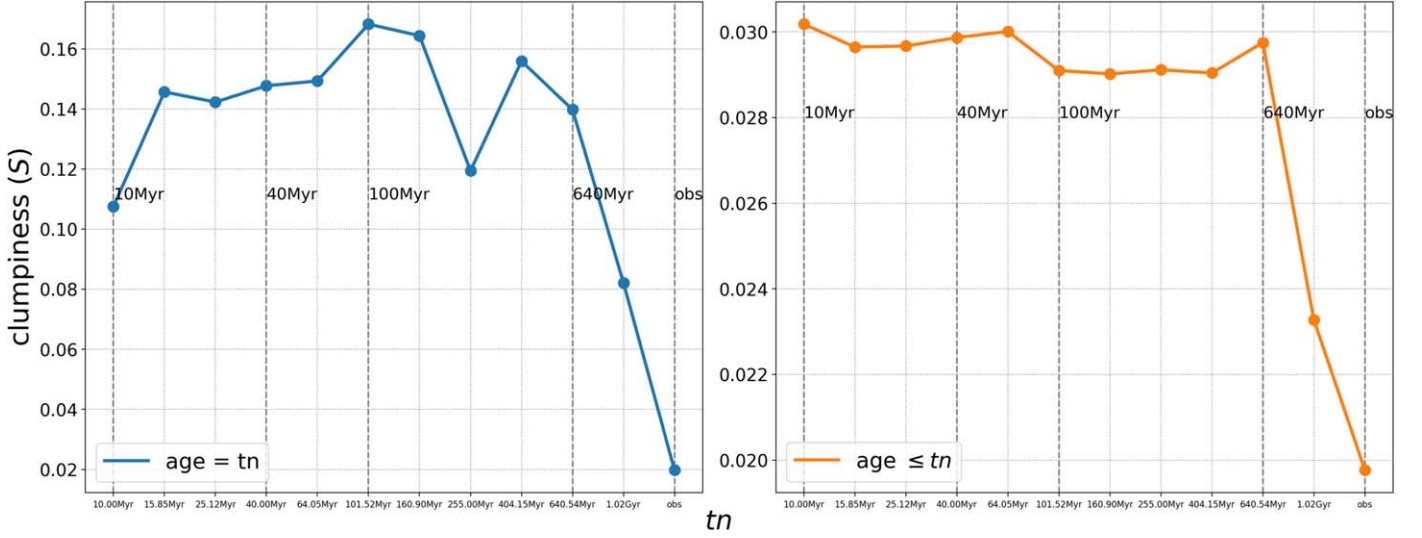


Figure 12. The clumpiness (S) of the g -band images of stellar populations across 11 age nodes ($age = tn$, left panel) and younger than these age nodes ($age \leq tn$, right panel), with various thresholds of ages. The S of the observed image is shown as the rightmost data point for each panel.

8257-3704 by analyzing the changes in the clumpiness factor in different age ranges.

The effective radius and the galaxy center of the old2 image are used to calculate S . S is summed over the spaxels from $0.25R_p$ to $2.0R_p$ in Equation (4). The width of the box is $0.25R_p$. Figure 12 shows the clumpiness of images for stellar populations in 11 different age intervals. The blue line represents the clumpiness of the g -band images with age equal to these age nodes ($age = tn$), and the orange line is the g -band images with age younger than these age nodes ($age \leq tn$). We also check the S of the g -band images older than these age nodes ($age \geq tn$), which have little clumpiness as expected. We find that the clumpiness is mainly greater in images with $age = 40.00$ Myr to 160.90 Myr, which agrees with the g -band images in Figure 11 in that the southeastern clump and the northwestern clump exist at the same time. The clumpinesses of the g -band images with $age = 404.15$ Myr and 640.54 Myr are slightly lower than the 160.90 Myr image, which may be caused by only the southeastern clump being formed in these age intervals. The clumpiness of the g -band images with age younger than 11 age intervals (the orange line in Figure 12) shows an inflection around 640 Myr. Summarizing from the above observations, we think the southeastern clump survived from nearly 600 Myr ago to 40 Myr ago and the northwestern clump formed nearly 100 Myr ago.

5. Summary

In this work, we apply the stellar population synthesis tool FADO and 90 SSPs to the spatially resolved spectra in five star-bursting dwarf galaxies, selected from the MaNGA survey to have off-centered clumps. The spatially resolved SFH obtained

from the analysis allows us to look back in time and study how the clumps and the hosts might have evolved. We find that the images of younger stellar populations of these galaxies are significantly more asymmetric and clumpier than the images of stellar populations older than 1 Gyr. Most of the clumps in the five galaxies appeared around hundreds of millions of years ago. In some of the five galaxies, there are multiple clumps which appear at different locations and even different ages. 8257-3704 is particularly interesting as its southeastern clump is only visible in the images of the stellar populations of 100 Myr–1 Gyr age, but not in the observed gri image. We experiment with constructing the g -band images of the stellar populations of refined age intervals by sampling 11 stellar population ages between 10 Myr and 1 Gyr. We find that this galaxy may have experienced two significant starburst events. The first one occurred around 600 Myr ago and ended around 40 Myr ago, while the second starburst event occurred within the last 100 Myr.

We also construct images of stellar populations older than certain ages to probe the properties and evolution of the hosts. These images allow us to probe the evolutionary connections between these star-bursting dwarf galaxies and other types of dwarfs, such as dEs and dIrrs, in a novel way that had not been fully explored before. We divide the stellar populations into three age intervals (≥ 10 Myr, ≥ 100 Myr, ≥ 1 Gyr), trying to capture the galaxies before their significant star formation events which may have occurred at different epochs. We use GALFIT to fit the surface brightness profiles of these “host” galaxies and then compare their structural parameters with those of other types of dwarf galaxies. We find that the B -band central surface brightness and effective radii of these five

galaxies, when plotted against their B -band magnitude, mainly fall between the regions of dEs and dIrrs. Among them, 8313-1901 and 8615-1901 are closer in their properties to dEs, while 9894-9102 is closer to dIrrs. We speculate that 8313-1901 was a dwarf elliptical galaxy before it accreted gas and formed its current star-forming clump around 10 Myr ago.

By applying the spectral synthesis methods to the IFU data, we are able to obtain the images of galaxies in different age intervals and spatially resolve the SFH. From these five galaxies, we find that this method allows us to acquire more characteristics and evolutionary history of both the host galaxies and clumps in star-bursting galaxies. This method can be applied to larger samples of galaxies of various types. With observations of higher spatial IFU instrumentation such as the IFS onboard the Chinese Space Station Telescope, we may also use the method to resolve and analyze the stellar population evolution of the star-forming clumps. These analyses will enhance our understanding of galaxy evolution further in the future.

Acknowledgments

This work was supported by National Key R&D Program of China (Nos. 2019YFA0405501 and 2022YFF0503402), and the National Natural Science Foundation of China (NSFC, Nos. 12233005 and 12041302). J.Y. acknowledges support from the Natural Science Foundation of Shanghai (Project Number: 22ZR1473000) and the Program of Shanghai Academic Research Leader (No. 22XD1404200). Y.R. acknowledges supports from the CAS Pioneer Hundred Talents Program, USTC Research Funds of the Double First-Class Initiative, as well as the NSFC grant 12273037. J.W. acknowledges the NSFC grants 12033004, 12333003. Z.S. acknowledges support from the NSFC through grants 12273091 and U2031139.

This work made use of the High Performance Computing Resource in the Core Facility for Advanced Research Computing at Shanghai Astronomical Observatory.

Funding for the Sloan Digital Sky Survey IV has been provided by the Alfred P. Sloan Foundation, the U.S. Department of Energy Office of Science, and the Participating Institutions. SDSS-IV acknowledges support and resources

from the Center for High-Performance Computing at the University of Utah. The SDSS website is www.sdss.org.

SDSS-IV is managed by the Astrophysical Research Consortium for the Participating Institutions of the SDSS Collaboration including the Brazilian Participation Group, the Carnegie Institution for Science, Carnegie Mellon University, Center for Astrophysics—Harvard & Smithsonian, the Chilean Participation Group, the French Participation Group, Instituto de Astrofísica de Canarias, The Johns Hopkins University, Kavli Institute for the Physics and Mathematics of the Universe (IPMU)/University of Tokyo, the Korean Participation Group, Lawrence Berkeley National Laboratory, Leibniz Institut für Astrophysik Potsdam (AIP), Max-Planck-Institut für Astronomie (MPIA Heidelberg), Max-Planck-Institut für Astrophysik (MPA Garching), Max-Planck-Institut für Extraterrestrische Physik (MPE), National Astronomical Observatories of China, New Mexico State University, New York University, University of Notre Dame, Observatório Nacional/MCTI, The Ohio State University, Pennsylvania State University, Shanghai Astronomical Observatory, United Kingdom Participation Group, Universidad Nacional Autónoma de México, University of Arizona, University of Colorado Boulder, University of Oxford, University of Portsmouth, University of Utah, University of Virginia, University of Washington, University of Wisconsin, Vanderbilt University, and Yale University.

Appendix

Fitting Results of Surface Brightness for the Other Four Galaxies

From Figures A1–A4, we present the g -band surface brightness profile fitting results of the host galaxies for 8313-1901, 8563-3704, 8615-1901 and 9894-9102 conducted using GALFIT. The first column includes the observed images, the stellar images, old1 images, old2 images and old3 images. The second column displays the model images given by GALFIT, while the third column exhibits the residual images. Table A1 provides the structural parameters, including g -band absolute magnitude (M_g), effective radii (R_e), Sérsic index (n) axis ratio (q) and position angle (PA), for these images as determined by GALFIT.

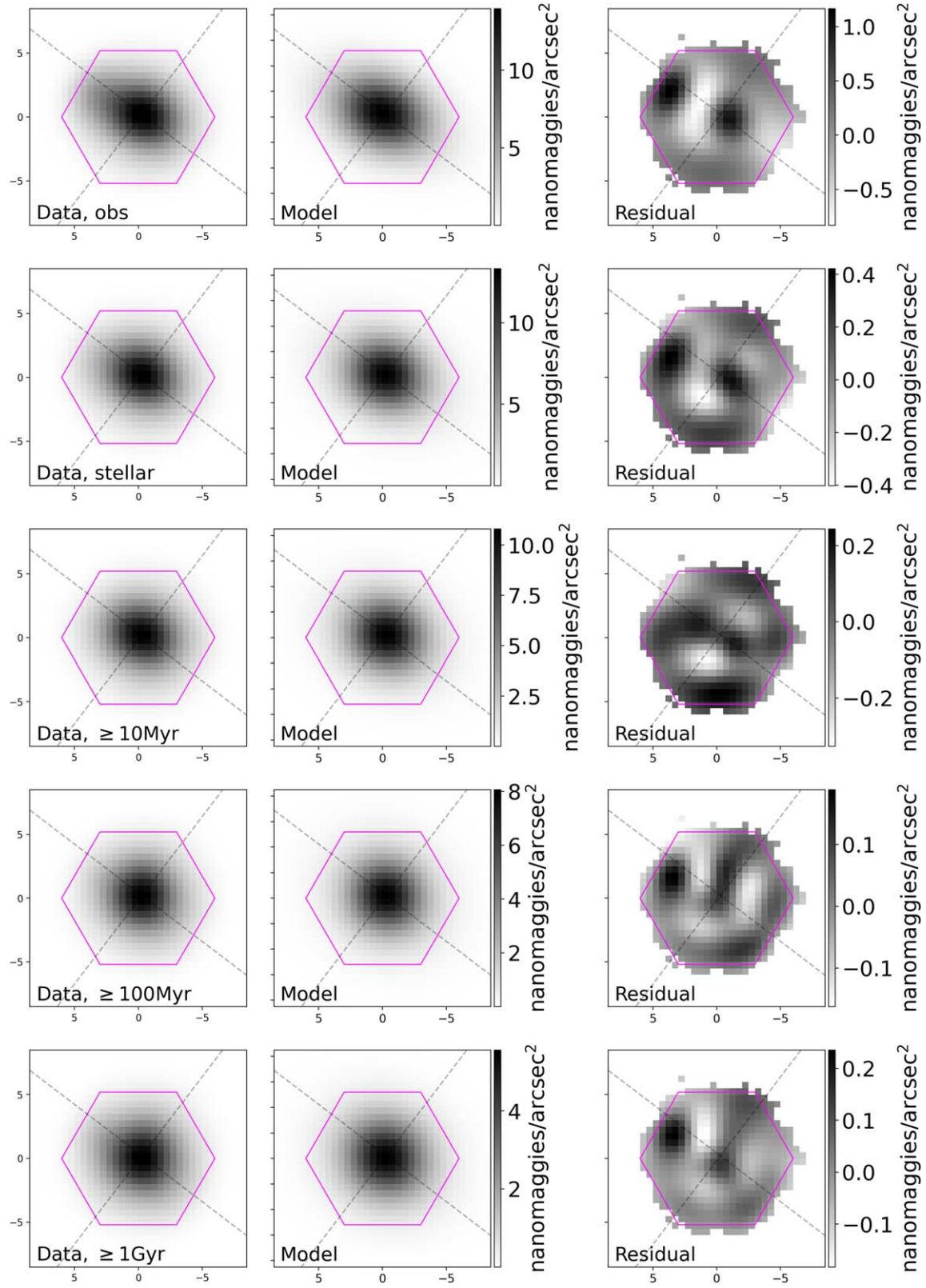


Figure A1. Two-dimensional surface brightness modeling of 8313-1901 with GALFIT.

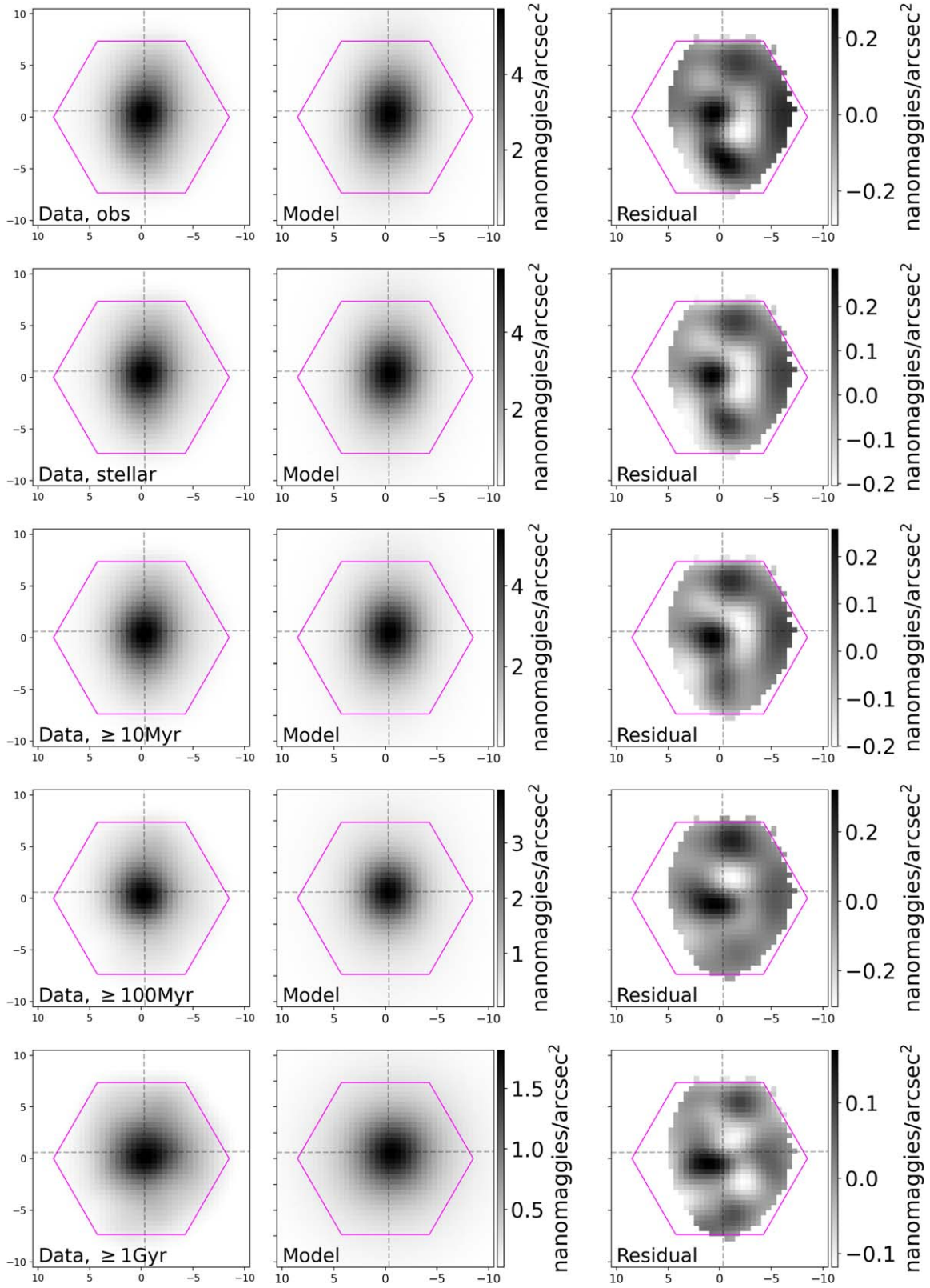


Figure A2. Two-dimensional surface brightness modeling of 8563-3704 with GALFIT.

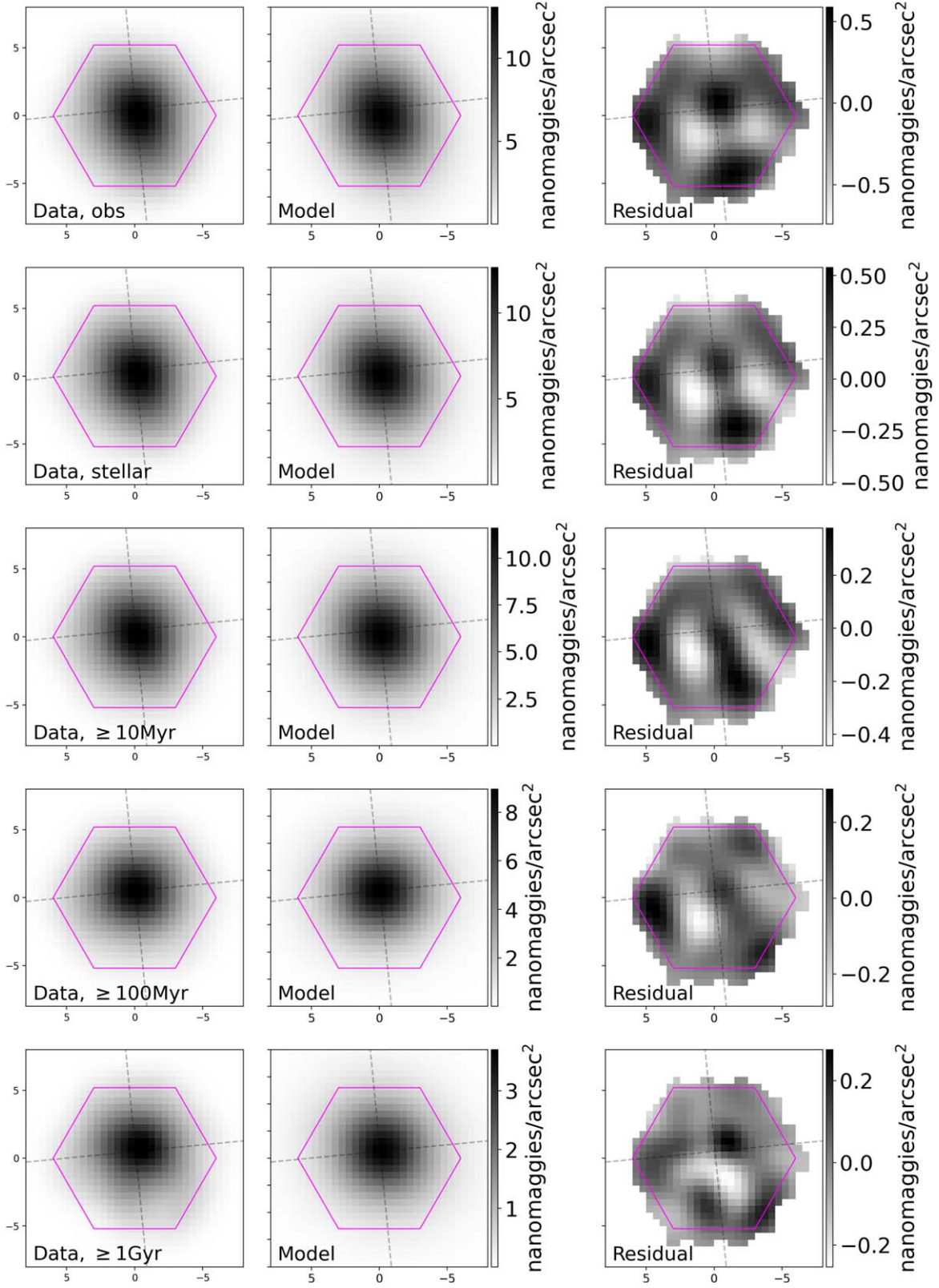


Figure A3. Two-dimensional surface brightness modeling of 8615-1901 with GALFIT.

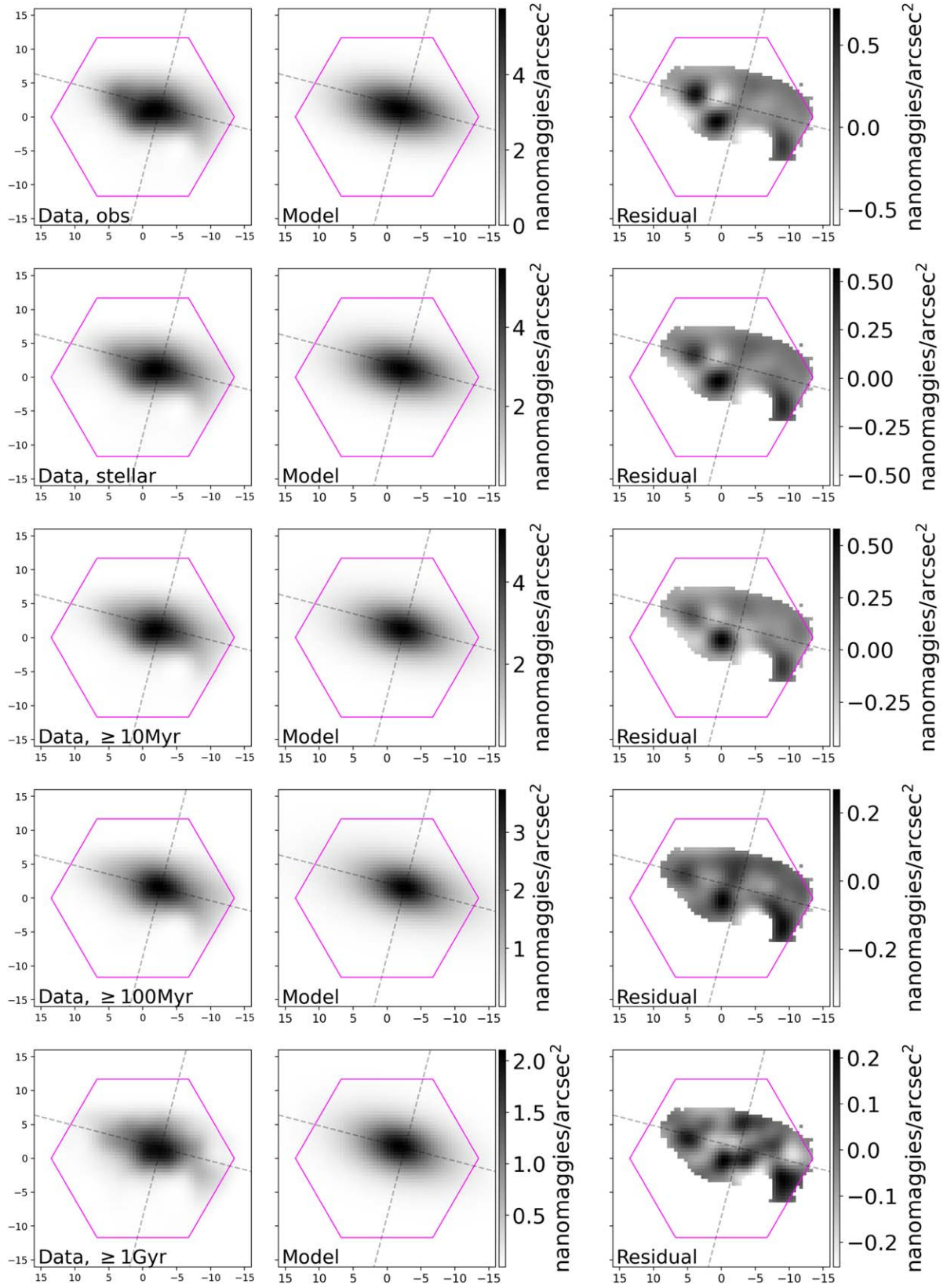


Figure A4. Two-dimensional surface brightness modeling of 9894-9102 with GALFIT.

Table A1
The Structural Parameters of the *g*-band Images of the Host Galaxies

Plateifu	M_g	R_e (kpc)	n	q	PA	Age
8257-3704	-17.06 ± 0.01	1.79 ± 0.06	0.70 ± 0.04	0.81 ± 0.01	-69.02 ± 0.84	old3 (≥ 1 Gyr)
	-17.13 ± 0.01	1.80 ± 0.06	0.63 ± 0.04	0.76 ± 0.01	-66.22 ± 0.73	old2 (≥ 100 Myr)
	-17.23 ± 0.01	1.81 ± 0.06	0.52 ± 0.03	0.73 ± 0.01	-64.79 ± 0.66	old1 (≥ 10 Myr)
	-17.33 ± 0.01	1.83 ± 0.06	0.48 ± 0.03	0.70 ± 0.01	-61.43 ± 0.50	stellar
	-17.58 ± 0.01	1.92 ± 0.07	0.47 ± 0.03	0.70 ± 0.01	-58.56 ± 0.99	observed
8313-1901	-17.50 ± 0.03	1.14 ± 0.04	0.98 ± 0.08	0.83 ± 0.01	57.48 ± 0.97	old3 (≥ 1 Gyr)
	-17.78 ± 0.01	1.00 ± 0.04	1.31 ± 0.06	0.83 ± 0.01	52.69 ± 0.86	old2 (≥ 100 Myr)
	-18.07 ± 0.01	1.03 ± 0.04	1.18 ± 0.07	0.72 ± 0.01	63.01 ± 0.58	old1 (≥ 10 Myr)
	-18.29 ± 0.01	1.10 ± 0.04	1.30 ± 0.07	0.62 ± 0.01	63.67 ± 0.48	stellar
	-18.65 ± 0.01	1.32 ± 0.04	0.83 ± 0.09	0.61 ± 0.01	62.52 ± 0.57	observed
8563-3704	-16.74 ± 0.03	2.06 ± 0.21	1.63 ± 0.06	0.95 ± 0.01	-7.00 ± 0.44	old3 (≥ 1 Gyr)
	-17.44 ± 0.05	2.21 ± 0.38	2.98 ± 0.08	0.73 ± 0.01	-5.19 ± 0.39	old2 (≥ 100 Myr)
	-17.41 ± 0.01	1.61 ± 0.10	1.47 ± 0.04	0.61 ± 0.02	-4.69 ± 0.4	old1 (≥ 10 Myr)
	-17.48 ± 0.01	1.67 ± 0.10	1.43 ± 0.04	0.58 ± 0.01	0.23 ± 1.16	stellar
	-17.74 ± 0.01	1.66 ± 0.09	1.20 ± 0.05	0.61 ± 0.01	-25.4 ± 6.20	observed
8615-1901	-16.89 ± 0.03	1.15 ± 0.07	1.05 ± 0.06	0.89 ± 0.01	58.36 ± 2.68	old3 (≥ 1 Gyr)
	-17.77 ± 0.02	1.08 ± 0.05	0.89 ± 0.04	0.86 ± 0.01	-84.42 ± 1.06	old2 (≥ 100 Myr)
	-18.11 ± 0.02	1.13 ± 0.05	0.73 ± 0.03	0.87 ± 0.01	33.62 ± 1.16	old1 (≥ 10 Myr)
	-18.22 ± 0.01	1.17 ± 0.05	0.72 ± 0.04	0.82 ± 0.01	27.48 ± 0.90	stellar
	-18.26 ± 0.01	1.29 ± 0.05	0.70 ± 0.04	0.81 ± 0.01	25.32 ± 0.94	observed
9894-9102	-17.24 ± 0.04	2.76 ± 0.06	0.82 ± 0.04	0.47 ± 0.01	74.49 ± 0.40	old3 (≥ 1 Gyr)
	-17.94 ± 0.04	3.21 ± 0.06	1.02 ± 0.03	0.40 ± 0.01	75.42 ± 0.20	old2 (≥ 100 Myr)
	-18.22 ± 0.04	2.86 ± 0.05	0.84 ± 0.03	0.42 ± 0.01	76.73 ± 0.22	old1 (≥ 10 Myr)
	-18.32 ± 0.01	2.92 ± 0.05	0.72 ± 0.02	0.42 ± 0.01	77.78 ± 0.23	stellar
	-18.36 ± 0.01	2.92 ± 0.05	0.61 ± 0.02	0.43 ± 0.01	75.09 ± 0.23	observed

ORCID iDs

Mengting Ju  <https://orcid.org/0000-0002-5815-2387>

Jun Yin  <https://orcid.org/0000-0002-4499-1956>

Lei Hao  <https://orcid.org/0000-0003-2478-9723>

Chenxu Liu  <https://orcid.org/0000-0001-5561-2010>

Chao-Wei Tsai  <https://orcid.org/0000-0002-9390-9672>

Junfeng Wang  <https://orcid.org/0000-0003-4874-0369>

Zhengyi Shao  <https://orcid.org/0000-0001-8611-2465>

Shuai Feng  <https://orcid.org/0000-0002-9767-9237>

Yu Rong  <https://orcid.org/0000-0002-2204-6558>

References

- Alloin, D., Collin-Souffrin, S., Joly, M., & Vigroux, L. 1979, *A&A*, **78**, 200
- Amorín, R., Aguerri, J. A. L., Muñoz-Tuñón, C., & Cairós, L. M. 2009, *A&A*, **501**, 75
- Annibali, F., Cignoni, M., Tosi, M., et al. 2013, *AJ*, **146**, 144
- Baldwin, J. A., Phillips, M. M., & Terlevich, R. 1981, *PASP*, **93**, 5
- Belfiore, F., Westfall, K. B., Schaefer, A., et al. 2019, *AJ*, **158**, 160
- Binggeli, B., & Cameron, L. M. 1993, *A&AS*, **98**, 297
- Blanton, M. R., Bershad, M. A., Abolfathi, B., et al. 2017, *AJ*, **154**, 28
- Bruzual, G., & Charlot, S. 2003, *MNRAS*, **344**, 1000
- Bundy, K., Bershad, M. A., Law, D. R., et al. 2015, *ApJ*, **798**, 7
- Cairós, L. M., Caon, N., Papaderos, P., et al. 2003, *ApJ*, **593**, 312
- Cairós, L. M., Vilchez, J. M., González Pérez, J. N., Iglesias-Páramo, J., & Caon, N. 2001, *ApJS*, **133**, 321
- Calzetti, D. 2001, *PASP*, **113**, 1449
- Ceverino, D., Dekel, A., & Bournaud, F. 2010, *MNRAS*, **404**, 2151
- Conselice, C. J. 2003, *ApJS*, **147**, 1
- Conselice, C. J., Blackburne, J. A., & Papovich, C. 2005, *ApJ*, **620**, 564
- Denicoló, G., Terlevich, R., & Terlevich, E. 2002, *MNRAS*, **330**, 69
- Elmegreen, B. G., Elmegreen, D. M., Sánchez Almeida, J., et al. 2013, *ApJ*, **774**, 86
- Elmegreen, B. G., Zhang, H.-X., & Hunter, D. A. 2012, *ApJ*, **747**, 105
- Elmegreen, D. M., Elmegreen, B. G., & Hirst, A. C. 2004, *ApJL*, **604**, L21
- Erb, D. K., Shapley, A. E., Pettini, M., et al. 2006, *ApJ*, **644**, 813
- Fagotto, F., Bressan, A., Bertelli, G., & Chiosi, C. 1994a, *A&AS*, **104**, 365
- Fagotto, F., Bressan, A., Bertelli, G., & Chiosi, C. 1994b, *A&AS*, **105**, 29
- Fitzpatrick, E. L. 1999, *PASP*, **111**, 63
- Genzel, R., Tacconi, L. J., Eisenhauer, F., et al. 2006, *Natur*, **442**, 786
- Gil de Paz, A., Madore, B. F., & Pevunova, O. 2003, *ApJS*, **147**, 29
- Gomes, J. M., & Papaderos, P. 2017, *A&A*, **603**, A63
- Graham, A. W., & Guzmán, R. 2003, *AJ*, **125**, 2936
- Gunn, J. E., Siegmund, W. A., Mannery, E. J., et al. 2006, *AJ*, **131**, 2332
- Hao, C.-N., Kennicutt, R. C., Johnson, B. D., et al. 2011, *ApJ*, **741**, 124
- Henry, A., Martin, C. L., Finlator, K., & Dressler, A. 2013, *ApJ*, **769**, 148
- Hunter, D. A., & Hoffman, L. 1999, *AJ*, **117**, 2789
- Izotov, Y. I., Guseva, N. G., & Thuan, T. X. 2011, *ApJ*, **728**, 161
- Jaskot, A. E., & Oey, M. S. 2013, *ApJ*, **766**, 91
- Johnson, B. D. 2019, SEDPY: Modules for Storing and Operating on Astronomical Source Spectral Energy Distribution, Astrophysics Source Code Library, ascl:1905.026
- Ju, M., Yin, J., Liu, R., et al. 2022, *ApJ*, **938**, 96
- Kauffmann, G., Heckman, T. M., Tremonti, C., et al. 2003, *MNRAS*, **346**, 1055
- Kennicutt, R. C., & Evans, N. J. 2012, *ARA&A*, **50**, 531
- Kewley, L. J., Dopita, M. A., Sutherland, R. S., Heisler, C. A., & Trevena, J. 2001, *ApJ*, **556**, 121
- Krueger, H., Fritze-v. Alvensleben, U., & Loose, H. H. 1995, *A&A*, **303**, 41

- Lagos, P., Scott, T. C., Nigoche-Netro, A., et al. 2018, *MNRAS*, **477**, 392
- Law, D. R., Cherinka, B., Yan, R., et al. 2016, *AJ*, **152**, 83
- Law, D. R., Westfall, K. B., Bershady, M. A., et al. 2021, *AJ*, **161**, 52
- Law, D. R., Yan, R., Bershady, M. A., et al. 2015, *AJ*, **150**, 19
- Lian, J. H., Kong, X., Jiang, N., Yan, W., & Gao, Y. L. 2015, *MNRAS*, **451**, 1130
- Lotz, J. M., Primack, J., & Madau, P. 2004, *AJ*, **128**, 163
- Marino, R. A., Rosales-Ortega, F. F., Sánchez, S. F., et al. 2013, *A&A*, **559**, A114
- Masters, K. L., Stark, D. V., Pace, Z. J., et al. 2019, *MNRAS*, **488**, 3396
- McQuinn, K. B. W., Skillman, E. D., Cannon, J. M., et al. 2010, *ApJ*, **721**, 297
- Meyer, H. T., Lisker, T., Janz, J., & Papaderos, P. 2014, *A&A*, **562**, A49
- Mo, H., van den Bosch, F. C., & White, S. 2010, *Galaxy Formation and Evolution* (Cambridge: Cambridge Univ. Press)
- Pagel, B. E. J., Edmunds, M. G., Blackwell, D. E., Chun, M. S., & Smith, G. 1979, *MNRAS*, **189**, 95
- Papaderos, P., Guseva, N. G., Izotov, Y. I., & Fricke, K. J. 2008, *A&A*, **491**, 113
- Papaderos, P., Loose, H. H., Fricke, K. J., & Thuan, T. X. 1996, *A&A*, **314**, 59
- Pappalardo, C., Cardoso, L. S. M., Michel Gomes, J., et al. 2021, *A&A*, **651**, A99
- Peng, C. Y., Ho, L. C., Impey, C. D., & Rix, H.-W. 2002, *AJ*, **124**, 266
- Peng, C. Y., Ho, L. C., Impey, C. D., & Rix, H.-W. 2010, *AJ*, **139**, 2097
- Peterken, T. G., Merrifield, M. R., Aragón-Salamanca, A., et al. 2019, *NatAs*, **3**, 178
- Pettini, M., & Pagel, B. E. J. 2004, *MNRAS*, **348**, L59
- Rey, S.-C., Kim, S., Chung, J., & Lee, Y. 2023, *ApJ*, **945**, 140
- Salzer, J. J., MacAlpine, G. M., & Boroson, T. A. 1989, *ApJS*, **70**, 447
- Sánchez Almeida, J., Caon, N., Muñoz-Tuñón, C., Filho, M., & Cerviño, M. 2018, *MNRAS*, **476**, 4765
- Sánchez Almeida, J., Morales-Luis, A. B., Muñoz-Tuñón, C., et al. 2014, *ApJ*, **783**, 45
- Sánchez Almeida, J., Muñoz-Tuñón, C., Amorín, R., et al. 2008, *ApJ*, **685**, 194
- Searle, L., & Sargent, W. L. W. 1972, *ApJ*, **173**, 25
- Smee, S. A., Gunn, J. E., Uomoto, A., et al. 2013, *AJ*, **146**, 32
- Smith, J. A., Tucker, D. L., Kent, S., et al. 2002, *AJ*, **123**, 2121
- Stark, D. V., Masters, K. L., Avila-Reese, V., et al. 2021, *MNRAS*, **503**, 1345
- Storchi-Bergmann, T., Calzetti, D., & Kinney, A. L. 1994, *ApJ*, **429**, 572
- Tosi, M. 2009, in *IAU Symp.*, **258**, 61
- Tremonti, C. A., Heckman, T. M., Kauffmann, G., et al. 2004, *ApJ*, **613**, 898
- van Zee, L. 2000, *AJ*, **119**, 2757
- Verbeke, R., De Rijcke, S., Koleva, M., et al. 2014, *MNRAS*, **442**, 1830
- Westfall, K. B., Cappellari, M., Bershady, M. A., et al. 2019, *AJ*, **158**, 231
- Yan, R., Bundy, K., Law, D. R., et al. 2016a, *AJ*, **152**, 197
- Yan, R., Tremonti, C., Bershady, M. A., et al. 2016b, *AJ*, **151**, 8
- Zhang, H.-X., Hunter, D. A., Elmegreen, B. G., Gao, Y., & Schruha, A. 2012, *AJ*, **143**, 47
- Zhang, H.-X., Smith, R., Oh, S.-H., et al. 2020, *ApJ*, **900**, 152